LLE Review

Quarterly Report

April–June 1990

UR
LLE

LLE Review

Quarterly Report

April–June 1990

UR
LLE

IN BRIEF

This volume of the LLE Review, covering the period April–June 1990, contains articles in two main sections, (1) Progress in Laser Fusion and (2) Advanced Technology Developments. The first article in Sec. (1) presents the theoretical interpretation of the glass-ablator cryogenic-implosion experiments recently conducted on OMEGA. It is followed by an article describing the analysis of neutron time-of-flight data taken during DT and DD experiments; and a discussion of the improvements to laser diagnostics that now provide for precise control of the OMEGA laser closes out Sec. (1). Section (2) contains a report on the development of transparent conductive coatings for KDP crystals, and a discussion of the study of the transient-surface Debye-Waller effect in materials irradiated with an ultrafast laser.

The highlights of this issue are

• Simulations of direct-drive, high-gain capsule designs have shown that thick, frozen-DT-fuel layers and low-atomic-number ablators are requirements for optimal performance. A series of direct-drive laser-fusion experiments using DT-filled cryogenically cooled glass-ablator capsules has been performed on the OMEGA 24-beam, 351-nm laser system. We present our latest understanding of the observed departures from predicted one-dimensional performance with respect to both neutron yield and ρR_f.

- The fuel-ion temperature for DD and DT target implosions can be determined from the neutron-energy spectrum obtained with a neutron time-of-flight (TOF) detector. A Monte Carlo model method of statistical error analysis has been developed to unfold the neutron-energy spectrum from the observed signal and extract the fuel-ion temperature.

- The current experiments relevant to the demonstration of inertial confinement fusion require that the target driver be capable of precise control. The OMEGA laser has been through a series of improvements allowing the system to be configured for a specific set of target experiments. These improved techniques give a well-characterized and reproducible illumination pattern to an implosion target.

- Several types of electro-optic devices require electrodes that are both optically transparent and electrically conductive. Some devices, such as the longitudinal Pockels cell, require application of a transparent electrode to a thermally sensitive substrate of potassium dihydrogen phosphate (KDP). The applied coating must also have a high laser-damage threshold for the infrared (1054 nm). A technique for depositing transparent conductors using indium-tin oxide (ITO) with ion-assisted deposition (IAD) is described.

- In the study of the interactions of ultrafast lasers with surfaces and the subsequent reactions, a key parameter is the time evolution of the surface temperature. We demonstrate the utilization of picosecond time-resolved reflection high-energy electron diffraction (RHEED) as a surface-lattice temperature probe.

CONTENTS

Dr. Hani Elsayed-Ali, Scientist, assisted by John Herman and Elizabeth Murphy, graduate students, prepares to perform an experiment on surface dynamics when the sample is subjected to a picosecond laser pulse. The top few atomic layers of a single crystal are probed using the technique of picosecond reflection high-energy electron refraction (RHEED), which provides a time-resolved surface temperature probe.

Section 1
PROGRESS IN LASER FUSION

1.A Theoretical Interpretation of OMEGA Glass-Ablator Cryogenic Implosion Experiments

Simulations of direct-drive, high-gain capsule designs have shown that thick, frozen-DT-fuel layers and low-atomic-number ablators are requirements for optimal performance. However, current target-fabrication and handling limitations preclude the use of energy-scaled capsules of this type in current direct-drive experiments. The only targets now available that are capable of providing moderately thick, frozen fuel layers are high-pressure ($P_0 \geq 100$ atm), DT-filled glass microballoons. A series of direct-drive laser-fusion experiments using DT-filled cryogenically cooled glass-ablator capsules has been performed on the OMEGA 24-beam, 351-nm laser system.[1,2] These experiments, which represent a first attempt at studying the hydrodynamic behavior of cryogenic-fuel-layer capsules on OMEGA, resulted in the highest directly measured fuel areal densities (ρR_f) achieved to date using the direct-drive approach to inertial confinement fusion. However, significant departures from predicted one-dimensional (1-D) performance with respect to both neutron yield and ρR_f were observed.

In this article we present our latest understanding of the observed discrepancies. In the first section we briefly review the experimental conditions, experimental results, and the simulation methodology used in modeling these experiments. In the remaining sections we discuss possible causes for the departures from 1-D performance. We show that, based on our latest understanding, there is a potential for a classically Rayleigh-Taylor[3-5] unstable interface to develop within the DT-fuel layer during the

117

acceleration phase of the implosion, which we believe is the principal cause for the discrepancies between experiment and simulation.

Experiments and Results

Glass microballoons containing approximately equimolar mixtures of D and T at densities corresponding to 75- and 100-atm, room-temperature fill pressures were used in these experiments. (In this article we will restrict our discussion to the 100-atm fill implosion results only.) The target inner diameters were ~250 μm and the glass-ablator thicknesses varied between 3 and 10 μm. The targets were supported (using no glue) by four or five spider silks approximately 0.5 μm in diameter drawn across a copper U-shaped mount. The width and thickness of the copper mounts were constrained by the requirements that the mount fit in the liquid-He-cooled shroud and that it not obscure any OMEGA laser beams.[1] To provide additional mechanical stability, the mount assembly, including the target, was coated with 0.2 μm of parylene. A detailed description of the cryogenic-target cooling and positioning system used in these experiments is given in Ref. 1.

The capsules were irradiated with up to 1500 J of 351-nm laser light. The pulse shapes were approximately Gaussian with full-width-half-maxima (FWHM) in the 600-ps to 650-ps range. The cryogenic implosion experiments presented in this article were conducted using two (theoretically calculated) different on-target illumination conditions. The first series incorporated the use of a distributed phase plate[6] (DPP) in each beam of the OMEGA laser system before the final focus lens. The second series, performed six months later, involved the initial implementation of a new method to improve on-target illumination uniformity compatible with frequency-tripled glass laser systems [smoothing by spectral dispersion (SSD)].[7] The predicted levels of illumination nonuniformity for these two series of experiments are shown in Fig. 43.1.

Numerical simulations of the cryogenic implosion experiments were performed using the one- and two-dimensional hydrodynamic codes *LILAC* and *ORCHID*. Both codes contain Lagrangian hydrodynamics, a tabular equation of state (SESAME),[8] thermonuclear burn, multigroup fusion reaction particle transport, and multifrequency radiation transport. The opacities used in the multifrequency radiation transport are obtained by reducing the Los Alamos National Laboratory 2000-frequency-group, local thermodynamic equilibrium library[9] to a desired group structure. Laser energy deposition is modeled using a geometric optic[10] ray-trace algorithm with energy deposited by inverse bremsstrahlung along each ray path. Flux limitation[11] of the Spitzer-Härm electron thermal transport is incorporated as a "sharp cutoff."

Simulations of the actual implosion experiments were performed using the measured values of capsule dimensions, room-temperature fill pressures, incident laser energy, and laser pulse width. Measurements of the cryogenic-fuel-layer thickness, temperature, and residual vapor gas density were not

obtained during these experiments. However, the temperature of the cooling shroud was measured and was typically in the range between 6°K and 8°K. By assuming that the capsule and the shroud were near thermal equilibrium (turbulent gaseous helium providing the path for heat conduction), the capsule frozen-fuel-layer conditions could be inferred. (For the simulations presented in this article, an initial DT-solid-fuel density of 0.26 g/cm^3 was used.[12])
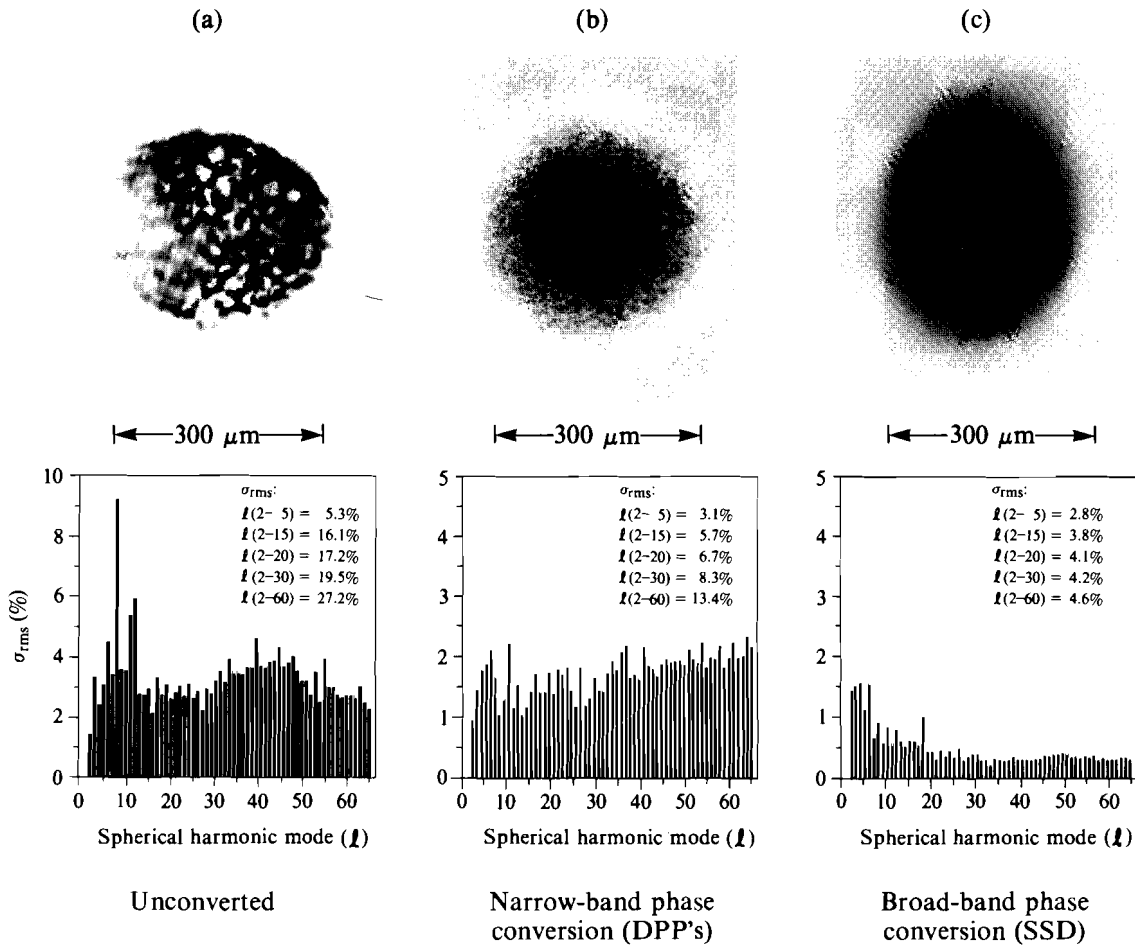
E5267

Fig. 43.1

Equivalent-target-plane distribution measured on one OMEGA beamline: (a) without DPP's, (b) with DPP's, (c) with SSD. The corresponding spherical-harmonic decompositions of overall uniformity on target, assuming 1% thermal smoothing, are shown underneath. Note the different scale on the bottom-left figure.

The density of the residual vapor gas at temperatures ≤ 8°K is extremely small[12] and was therefore neglected in the simulations presented here. However, this raises questions regarding the numerical treatment of the

void closure during the simulation and its potential influence on the predicted neutron production and capsule compression. One-dimensional simulations conducted for this study have shown that for a vast majority of the implosions modeled, the ion mean free path associated with the heating of the central fuel region at the time of void closure is short when compared to the size of the first fuel zone. Therefore, for the numerical results presented here, the kinetic energy associated with the inner fuel zone boundary is deposited into the ions of the first fuel zone at the time of void closure. To examine the sensitivity of this choice, 1-D calculations were conducted in which the kinetic energy of the inner fuel boundary was distributed over a number of inner fuel zones. These calculations showed a small yield reduction (less than a factor of 2) and a slight increase in the final neutron-weighted fuel and shell areal density when compared to the same cases in which the first zone dump of the kinetic energy was used. Simulations were also performed in which the residual vapor was modeled thereby avoiding the issues associated with void closure. Results from these calculations showed a small neutron-yield increase (approximately a factor of 2) and a slight decrease in the neutron-weighted areal densities when compared to the first zone kinetic-energy dump cases. Since the numerical simulations presented in the remaining sections were carried out in a similar manner we do not expect the issues associated with void closure to affect the interpretation of the trends in the experimental data; however, it could affect absolute comparisons for a particular simulation/shot.

The measured fuel areal density (neutron averaged) versus calculated convergence ratio and initial ablator thickness is shown in Figs. 43.2(a) and 43.2(b) respectively. The measured fuel-areal-density values were obtained using the "knock-on" diagnostic.[13–15] This diagnostic measures the number of deuterons and tritons in the compressed fuel elastically scattered by the 14.1-MeV neutrons emitted from the DT fusion reactions. The number of scattered "knock-on" ions is directly proportional to the fuel areal density. The possible presence of fuel-ablator mixing during neutron emission, while affecting the overall implosion dynamics, has little effect on the interpretation of the fuel areal density since only the elastically scattered fuel deuterons and tritons are measured. However, the areal-density value obtained does depend on the spatial extent of the neutron emission, which can be influenced by the presence of mixing during the stagnation phase of the implosion. [For example, for the same uniform (radial) fuel-density profile, a case in which the neutron emission was uniform throughout the fuel region would result in an inferred fuel areal density 4/3 higher than a case in which the neutron emission was from a central point source. In the cases presented here we have assumed that the neutron emission was from a central point source when determining ρR_f.] The normalized fuel ρR_f (measured ρR_f /1-D neutron-averaged fuel ρR) versus calculated convergence ratio and initial ablator thickness is displayed in Fig. 43.3(a) and 43.3(b). The calculated convergence ratio is defined as the initial fuel-ablator interface radius divided by the minimum radius of this interface during the implosion.
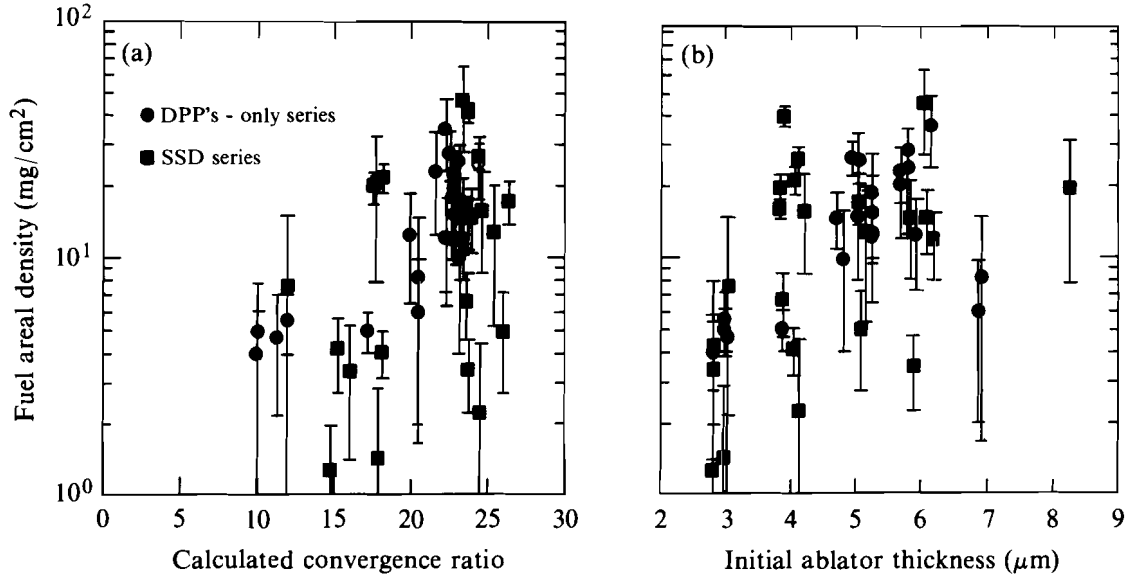
Fig. 43.2
Fuel areal density versus (a) calculated convergence ratio and (b) initial ablator thickness.
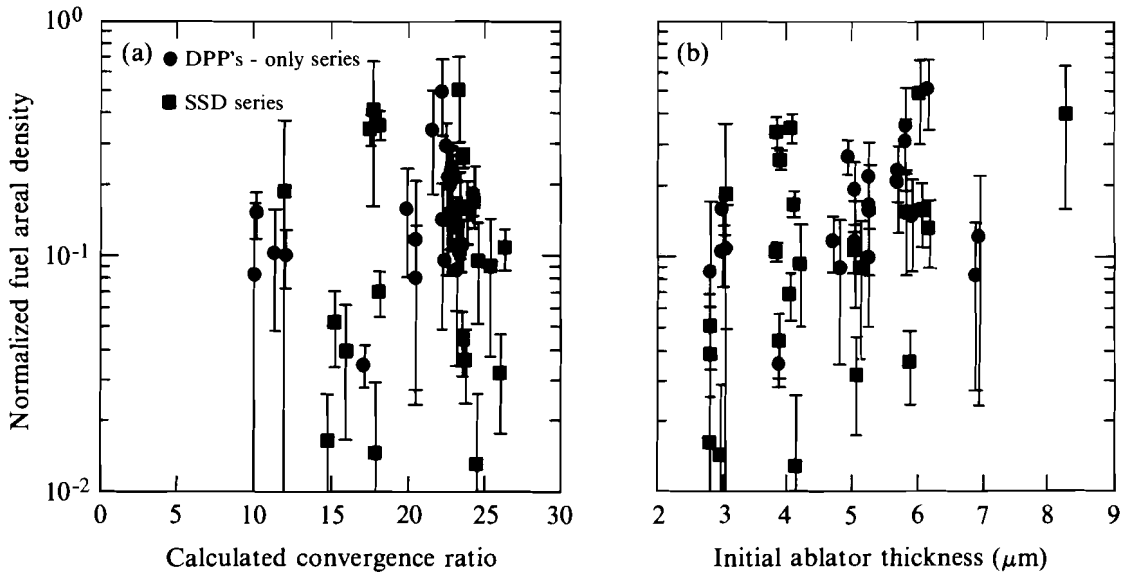
TC2785

Fig. 43.3
Normalized fuel areal density versus (a) calculated convergence ratio and (b) initial ablator thickness.

TC2786

Figure 43.3 shows that, for those data points with reasonable statistical uncertainty, the measured fuel areal density ranges between a factor of 2 to 50 below code predictions. The observed neutron yield obtained for these implosions ranged between 10^{-3} and 10^{-4} of the simulated 1-D neutron yield. In the following sections we attempt to identify the possible causes for these departures. The discussion will be divided as follows: (1) experimental and simulation agreement with measured acceleration-phase implosion characteristics; (2) effects of long-wavelength perturbations; (3) Rayleigh-Taylor unstable growth during the deceleration phase of the implosion; and (4) effects of Rayleigh-Taylor unstable growth during the acceleration phase of the implosion.

Acceleration Phase Comparisons

The first area of agreement is between experiments and simulations of the (large-scale) dynamics of a glass-ablator capsule during the acceleration phase of the implosion. A series of experiments was conducted to determine a value for the electron thermal-conduction flux limiter.[13] The experiments examined the absorbed laser energy and the fraction of x rays emitted using solid glass targets. The absorbed laser energy was measured with a set of 15 plasma calorimeters symmetrically arranged about the target chamber; the energy re-emitted as x rays was determined by a single differential x-ray calorimeter. The flux limiter was adjusted in the simulations until good agreement between the predicted and observed values for the absorbed laser energy was obtained over the incident laser intensity range of $\sim 10^{13}$–10^{15} W/cm^2. The flux-limiter value giving the best agreement was $f_e = 0.06$. Using this value, the x-ray conversion data also showed good agreement over this same intensity range. The same value of f_e, when used to model imploding glass-ablator capsules, was found to give agreement between measurements and simulation for the absorbed-laser-energy fraction and x-ray-conversion efficiencies to within ±5% over the same intensity range.

To further check our ability to simulate the coarse features of the hydrodynamic behavior during the acceleration phase, comparisons were made of the measured and predicted implosion time histories of glass-ablator capsules. These comparisons were carried out using a number of x-ray diagnostics. Figure 43.4 displays the implosion history of a 25-atm, D_2-filled, ~ 5-μm-thick glass-ablator capsule obtained using x-ray streak photography. To highlight the image structure, which is dominated by emission at the time of stagnation, two color cycles have been used on a nonlinear intensity scale. The solid lines, superimposed on the experimental image, show the *LILAC* prediction for the maximum-emission radius as a function of time. (Near the time of maximum compression, emission from the fuel core causes the calculated trajectory to jump to the axis.) Since the absolute timing was unknown on this shot, the relative timing between the experimental data and 1-D prediction has been adjusted to give the best fit. Up to the point of maximum compression, very good agreement exists between the experimental and predicted trajectories. However, after peak compression, departures can be noticed. The core is displaced (positive
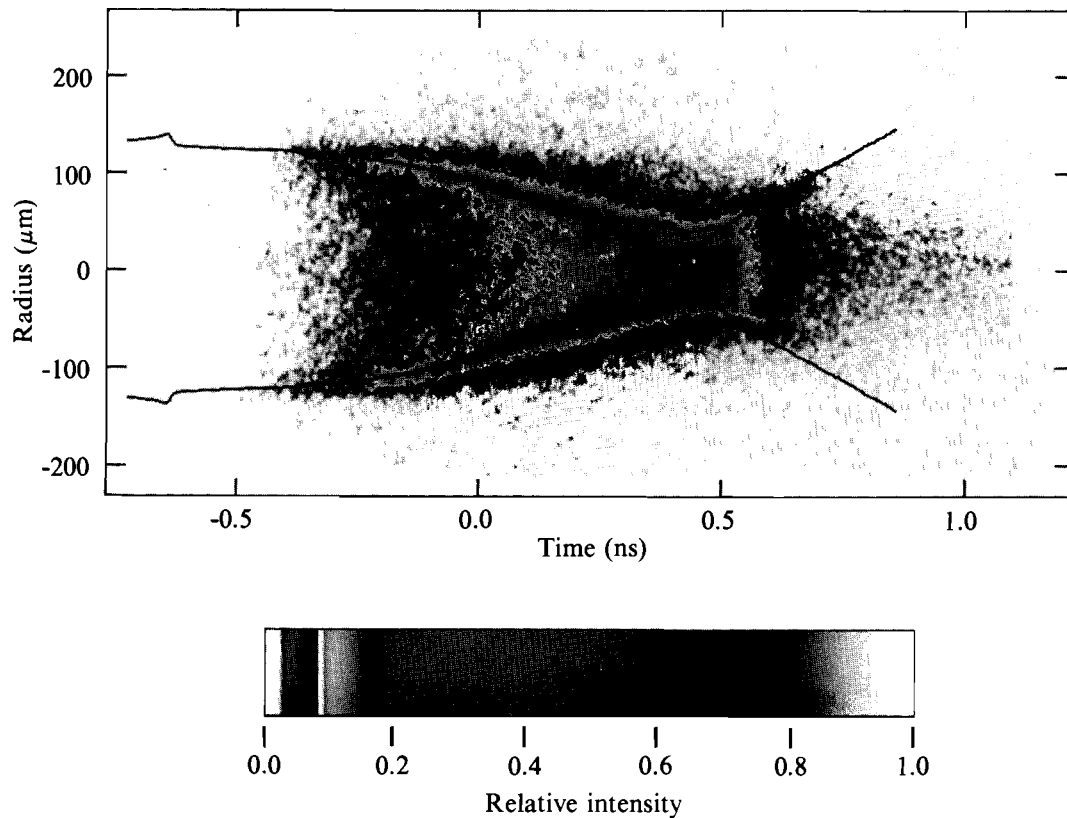
Fig. 43.4
Implosion history of a 25-atm, D_2-gas-filled capsule recorded by an x-ray-imaging streak camera. The trajectory of maximum x-ray emission calculated using *LILAC* is superposed (solid line).

radius direction in Fig. 43.4) and the upper disassembly trajectory ($r > 0$, Fig. 43.4) is in better agreement with the simulation than for the lower trajectory. Additional comparisons between simulations and experiments were made using the results obtained from an x-ray-framing camera.[16–18] The framing camera consisted of a pinhole camera assembly with an array of pinholes illuminating a gated microchannel plate. For the results shown here, the framing time was ~150-ps FWHM and the time between frames was ~250 ps. Figure 43.5 illustrates the agreement observed on cryogenic implosions for capsules of three different ablator thicknesses. Since no timing fiducial existed on the framing camera, the location of the first frame was selected to give the best agreement between experiment and simulation. Because the frame separation time is known, the placement of the remaining three frames is set by the location of the first. Figure 43.5 shows good agreement during the acceleration phase between simulation and experiment for the three ablator thicknesses.
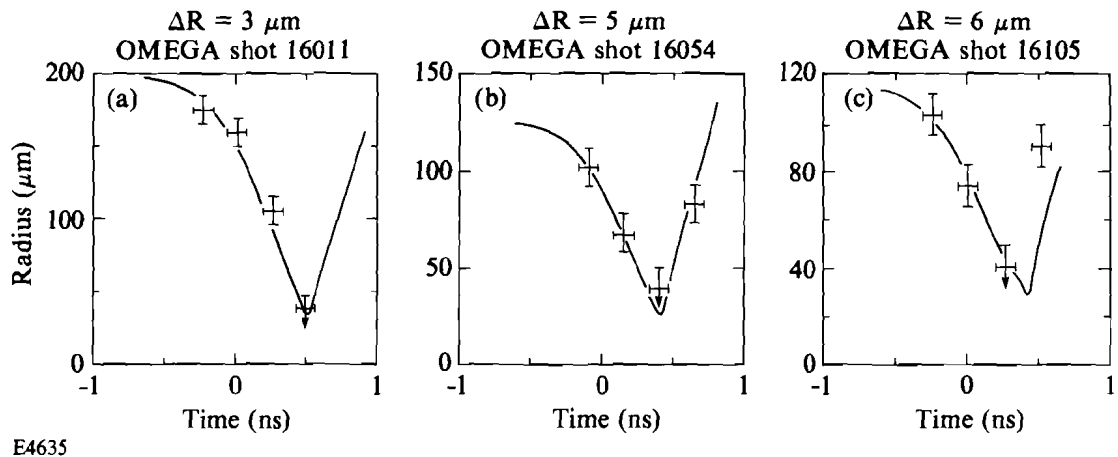
Fig. 43.5
Radius of peak x-ray emission versus time determined from framed x-ray images for three cryogenic capsules having (a) 3-μm, (b) 5-μm, and (c) 6-μm initial ablator thickness. *LILAC* predictions of the same implosions are shown as solid lines. Times are with respect to the peak of the laser pulse.

The comparisons of absorbed laser energy, x-ray energy conversion, and implosion time history (using $f_e = 0.06$) show that our numerical simulations are able to predict the coarse features of the dynamic of imploding glass-ablator capsules during the acceleration phase. This implies that no large discrepancies exist between simulation and experiments on the energy amount available in the shell to compress and heat the fuel during the final stages of the implosion.

Having found agreement between the experiments and code predictions during the acceleration phase of the implosion, we now address issues that could result in the observed departures of the neutron yield and fuel areal density from 1-D predictions. These possible causes for departure cannot be quantitatively measured, except for their influence on the final core conditions, using diagnostics currently available on the OMEGA system.

Long-Wavelength Perturbations

The presence of long-wavelength perturbations during the capsule implosion represents a possible source of disagreement between experiment and calculations. These long-wavelength perturbations were predominantly from variations in the frozen-fuel-layer thickness and laser power imbalance between the individual laser beams. Three sources of power imbalance have been identified for the OMEGA laser system.[19] The first arises from the state of polarization in each beam as it enters its third-harmonic conversion crystal, the second involves energy balance. The third source depends on the flux levels in each of the OMEGA laser amplifiers. Each of the sources modifies the shape of the laser pulse, resulting in the potential for long-wavelength ($\ell \leq 4$) modes of on-target illumination nonuniformity whose amplitude as well as modal content can change in time. Simulations

of experiments conducted only with DPP's showed that power imbalances, of the types discussed above, may have resulted in on-target illumination nonuniformities of ~40% peak-to-valley, in modes $1 \leq \ell \leq 4$, during the early portion of the implosion. (Between the DPP and SSD series of cryogenic implosion experiments the first two sources of power imbalance were improved on OMEGA. Work is still underway on the third source at this time.) Two-dimensional (2-D) *ORCHID* simulations have shown that these levels of long-wavelength illumination nonuniformity would dominate the possible effects of the measured, $\ell \leq 2$, fuel-layer-thickness variations. To examine a "worst-case" situation, a 2-D simulation was carried out for which the level of illumination nonuniformity in modes $1 \leq \ell \leq 4$ was held fixed at 45% peak-to-valley over the duration of the laser pulse. Figure 43.6 displays the predicted fuel density of the imploded core at the time at which the simulated yield equals the measured yield for pellets of similar initial ablator thickness (~5 μm). Note that although only long-wavelength modes were initially applied, their nonlinear interactions during the final implosion stages have resulted in the generation of shorter-wavelength distortions in the fuel region. (When the same modes were applied with a peak-to-valley variation of only 10%, the strong mode-mode interactions were not observed; a Legendre decomposition of the fuel ρR showed that the dominant distortions remained.)
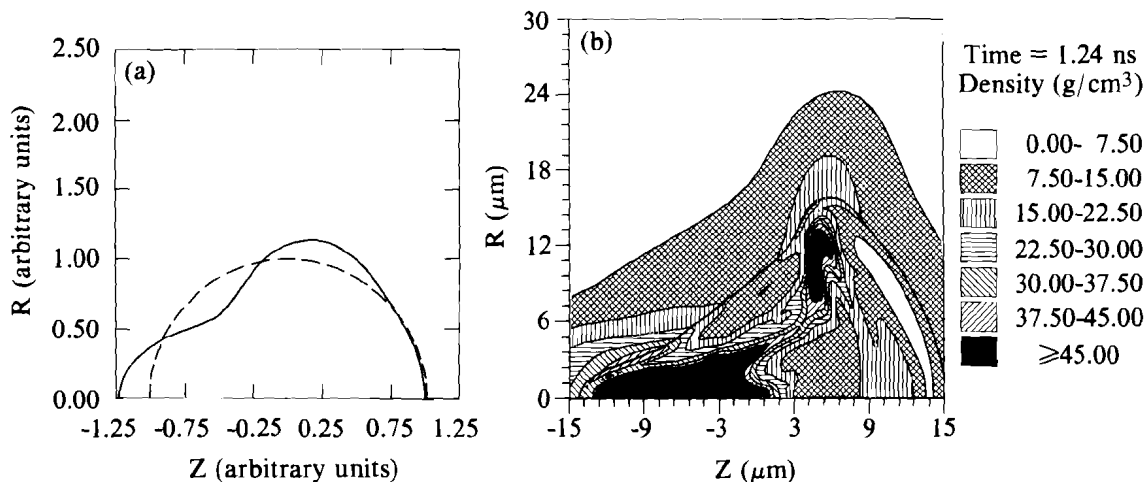
TC2549

Fig. 43.6
Two-dimensional (*ORCHID*) hydrodynamic simulation of a 5-μm-glass-ablator cryogenic implosion subjected to long-wavelength illumination nonuniformities.
(a) Illumination-nonuniformity pattern placed on target (solid line), modes $1 \leq \ell \leq 4$, peak-to-valley of ~45%.
(b) Density contours (g/cm^3) at the time when the simulation yield equaled the level of experimentally observed yield for similar-ablator-thickness capsules.

The 2-D simulations show that the predicted overall effect on cryogenic capsule performance of long-wavelength nonuniformities is a reduction of neutron yield by a factor of 2 to 10 for peak-to-valley variations in the 10%-to-45% range in modes $1 \leq \ell \leq 4$. This yield reduction is due to a lower efficiency of kinetic-to-internal energy conversion during the stagnation phase of the implosion. The neutron-weighted fuel areal density, while aspherical, is not appreciably changed from simulations carried out assuming perfect illumination uniformity. Depending on the modal content of the perturbation, the neutron-weighted ρR_f could be reduced due to an increased final fuel volume from the uniform case. However, in some cases, the ρR_f could also increase due to both cooler core conditions and a temporal shift of the neutron production such that the ρR_f is weighted toward a time when high fuel densities are present. (If all of the 45% peak-to-valley were placed in a pure $\ell = 2$, the effect on capsule performance would have been more substantial, especially with respect to the fuel areal density. However, numerical simulations of the potential power imbalance present on the OMEGA system during the DPP-only series show that the concentration of a majority of the resulting illumination nonuniformity in an $\ell = 2$ mode was highly unlikely.)

Rayleigh-Taylor Unstable Growth

The simulations in the previous section do not take into account the potential effects of fuel-ablator mixing during the deceleration (stagnation) phase of the implosion. Two possible sources could result in mixing of fuel and ablator material. For long-wavelength cases (see Fig. 43.6), mixing could occur due to shear and/or vortex-like flows that develop near the fuel-ablator interface. A second source of mixing could be driven by the development of Rayleigh-Taylor[17,18] unstable flow and convergence effects during the deceleration stage of the implosion.

For long-wavelength modes, *ORCHID* simulations show that while shear and vorticity-generated vortex flows would result in mixing of ablator and fuel material, the time and spatial scale of this mixing would not fully explain the experiments. The *ORCHID* simulations show that over ~90% of the neutron yield should be obtained before strong shear and vortex flows develop to any large extent. Therefore, since the simulation in Fig. 43.6 represents a "worst" case, we do not believe that long-wavelength perturbations explain the differences between experiment and simulation.

The potential effects of short-wavelength Rayleigh-Taylor instabilities during the deceleration phase of the implosion have been examined. One- and two-dimensional simulations have shown that there are two regions where Rayleigh-Taylor unstable flow should develop. The first region is a DT-DT "interface" between the hotter inner fuel and the surrounding colder fuel; the second is the fuel-ablator interface. *ORCHID* simulations of single modes (run in the small-amplitude, linear regime) show that both of these regions have essentially "classical" Rayleigh-Taylor growth rates, which can be approximated by the expression[20]

$$\gamma \approx \sqrt{A(t)kg(t)/[1+kL(t)]},$$ (1)

where $A(t)$ is the Atwood number, k is the unstable wave number, $g(t)$ is the acceleration, and $L(t)$ is a density scale length. The potential growth of all unstable modes and the subsequent mixing at the DT-DT unstable region, while possibly resulting in a neutron-yield reduction due to lower kinetic energy to thermal energy conversion, would not explain the observed reductions in fuel areal density and might, in some situations, result in higher ρR_f due to the cooling of the hotter DT region.

Mixing of fuel and ablator material due to unstable growth at the ablator-fuel interface has been examined using a simplified model. This model shows that while mixing of fuel and ablator material could potentially take place, the time and spatial scales are again insufficient to explain the departures in capsule performance. This can be seen by an analysis of the "free fall" trajectory of shell material into the fuel. The maximum penetration rate of ablator material into the fuel during the stagnation phase of the implosion is given by the glass-shell velocity at the fuel-glass interface at the time the shell begins to decelerate (assuming that no external forces act on the ablator material). Assuming the neutron production in a given zone is stopped as the free fall trajectory passes through that fuel zone, one can estimate the yield reduction that might take place due to mixing. Figures 43.7(a) and 43.7(b) show the results of this calculation for a 3-μm and a 6-μm ablator thickness. For these cases, essentially all of the yield occurs before mixing can quench it.
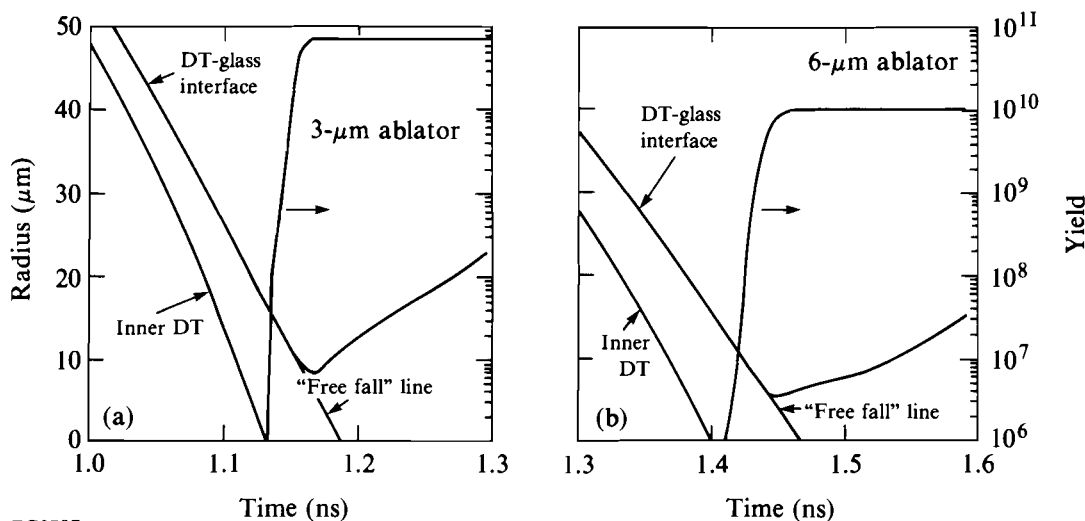
TC2787

Fig. 43.7
Radial location of the inner fuel edge, fuel-ablator interface, "free-fall" trajectory, and neutron yield (right-hand axis) versus time for a (a) 3-μm-glass-ablator and (b) 6-μm-glass-ablator cryogenic capsule implosion.

The effect of Rayleigh-Taylor unstable growth during the acceleration phase of the implosion was the last area to be examined. One- and two-dimensional simulations have shown a number of potential Rayleigh-Taylor unstable regions present during the acceleration phase of the glass-ablator cryogenic capsules. Figure 43.8 displays the pressure and density profiles at various times for an implosion using a 3-μm-thick ablator. Figure 43.8 shows that there are two unstable regions present during the acceleration phase. The first is located at the electron thermal-conduction-driven ablation surface, while the second is located within the DT fuel itself. (The unstable region in the DT is caused by the large differences in equation of state and opacities for DT and glass.) Two-dimensional *ORCHID* simulations of single-wavelength perturbations, calculated well within the small-amplitude, linear-growth region have shown that the Rayleigh-Taylor growth rates at the electron thermal-conduction-driven ablation surface can be approximated as

$$\gamma \approx \sqrt{A(t)kg(t)/[1+kL(t)]} - \beta kV_a(t), \tag{2}$$

where $V_a(t)$ is the ablation velocity and β is a constant that can range between 1 and 3 depending on the definitions used for $A(t)$, $L(t)$, and $V_a(t)$. *ORCHID* simulations show that the DT unstable interface is essentially "classical" modified by a small density-scale-length [$L(t)$] term [Eq. (1)]. When the ablator thickness becomes greater than ~4.5 μm, the simulations show that the situation, in terms of unstable interfaces, becomes more complicated. An additional unstable region evolves in the ablator associated with a radiation wave propagating into it. This feature is illustrated in Fig. 43.9 for an initially 5-μm-thick ablator. Two-dimensional simulations show that the unstable growth rates of this surface are greater than those of the electron thermal-conduction ablation surface but lower than the DT unstable region.

A modal analysis stability model similar to the one presented in Ref. 21 was used to examine the potential effects of all these unstable regions on pellet performance. *ORCHID* was run in the small amplitude linear region to determine the growth-rate spectrum for all the unstable regions for a given pellet implosion. These growth rates were then incorporated into the stability model to determine the potential amount of mix that could occur during the acceleration phase. The results show that the development of the DT unstable region plays the dominant role in these implosions. For capsules with initial ablator thickness ≳4.5 μm, the unstable region associated with the radiation wave is also important. However, for all ablator thicknesses considered, the model indicates that the growth at the DT unstable interface alone could result in substantial mixing of the DT fuel with ablator material during the acceleration phase.

Currently the multidimensional programs used for ICF implosion simulations are incapable of modeling all of the unstable modes of interest during an implosion. However, to at least determine if this unstable behavior could be the potential source for mixing during the acceleration

1.25-kJ, 625-ps Gaussian; $R_{ID} = 125 \ \mu m$
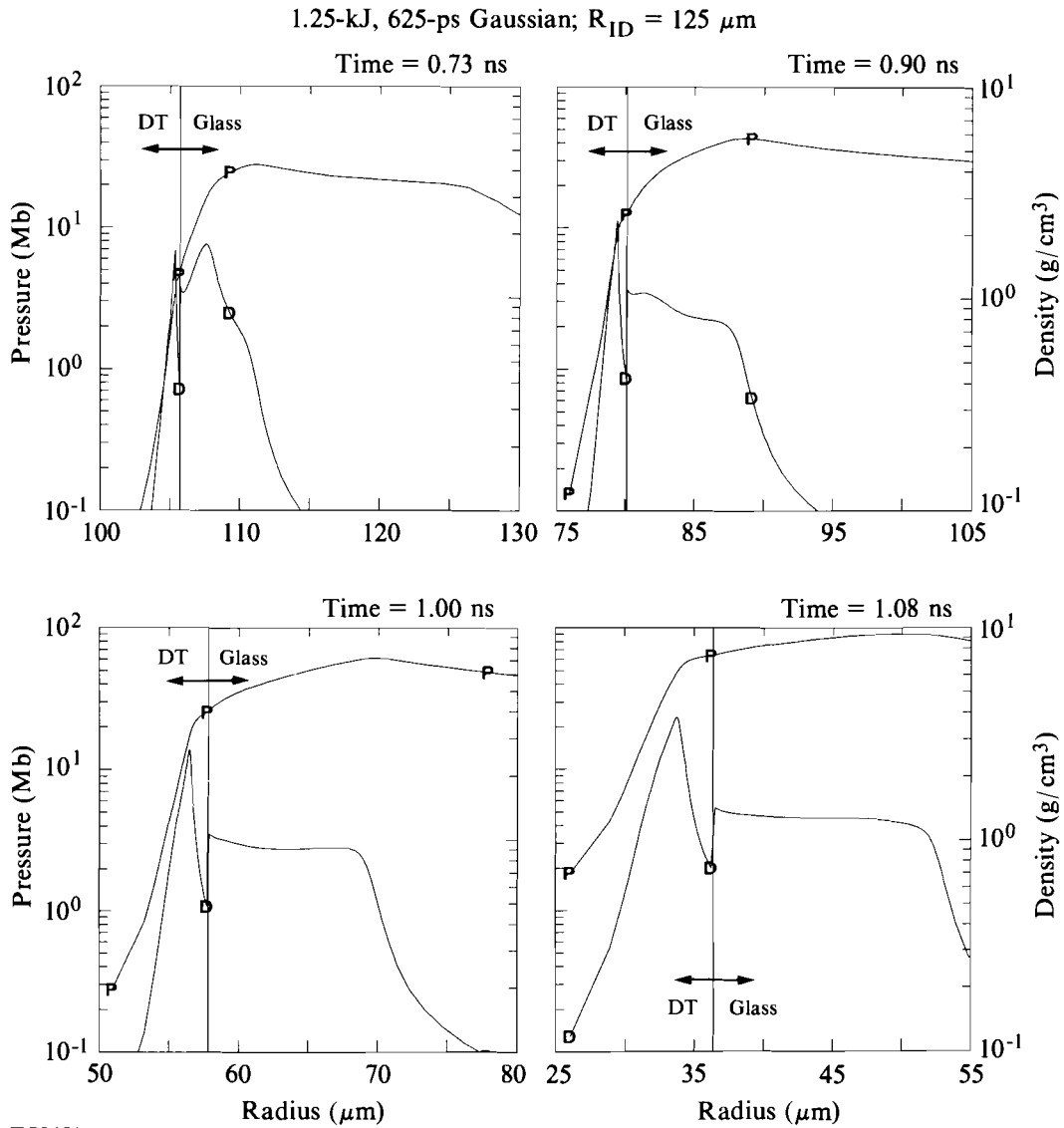
Fig. 43.8
Pressure and density profiles versus radius at various times for a 3-μm-glass-ablator cryogenic capsule implosion.

phase, a two-dimensional *ORCHID* simulation was conducted that considered the modes $2 \leq \ell \leq 20$ with a total illumination nonuniformity of ~15% peak-to-valley. Assuming DPP illumination only, this represents the illumination-nonuniformity level predicted (in these modes). Figure 43.10 displays the density conditions of the pellet at the time when the experimental and simulation yield are equal. The large distortions present at an average radius of 9 μm are due to the development of the DT unstable region during the acceleration phase. The seeds for this growth were transmitted from

1.25-kJ, 625-ps Gaussian; R_{ID} = 125 μm
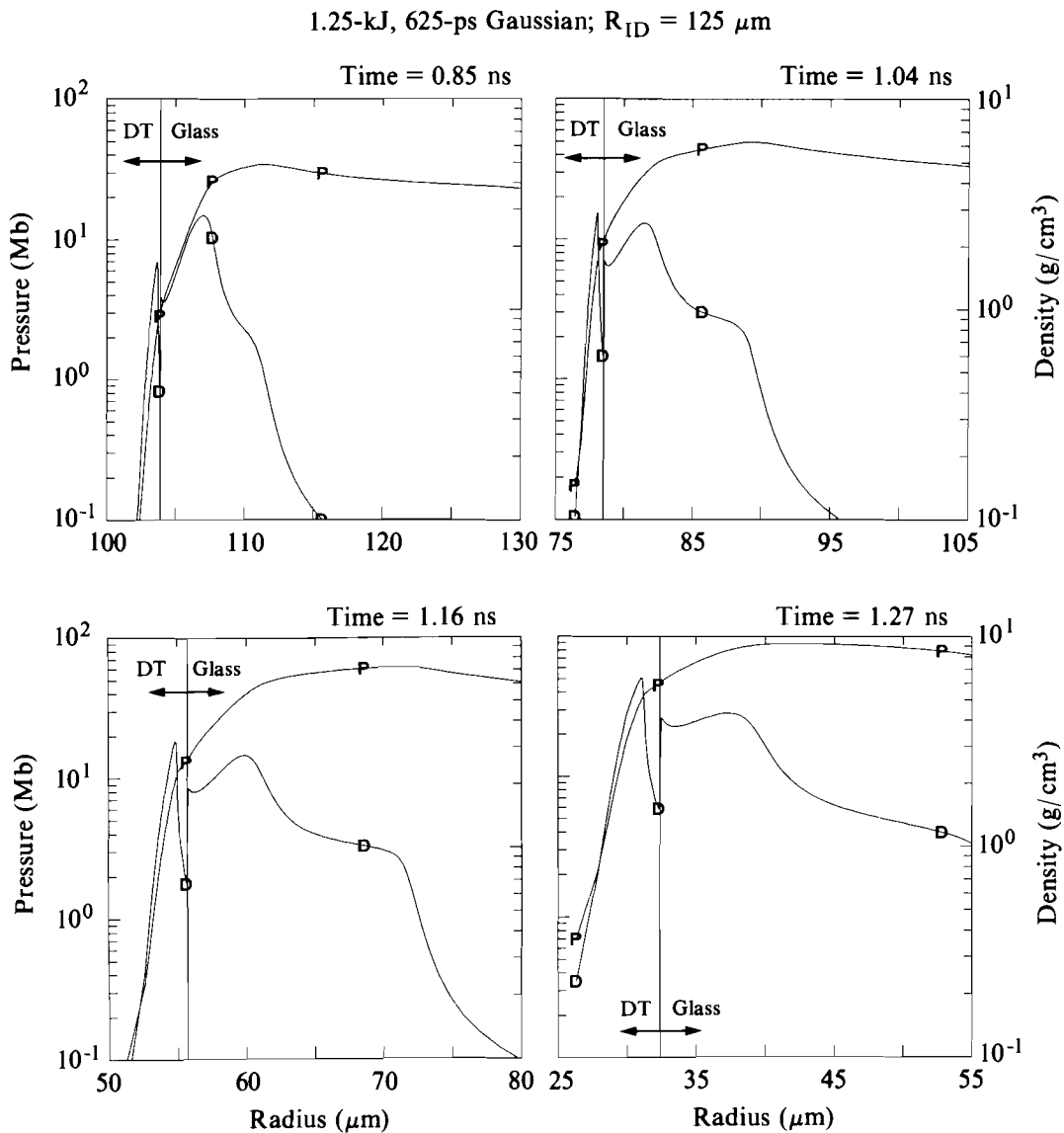
Fig. 43.9
Pressure and density profiles versus radius at various times for a 5-μm-glass-ablator cryogenic capsule implosion.

nonuniformities at the ablation surface during the implosion. The simulation shows that this surface has undergone a large amount of distortion and has resulted in mixing of fuel and ablator material before deceleration. Due to the limited number of modes considered, the mixing in this simulation is confined to the outer region of the fuel, and the calculated yield reduction is small, approximately a factor of 10 below the uniform illumination simulation.
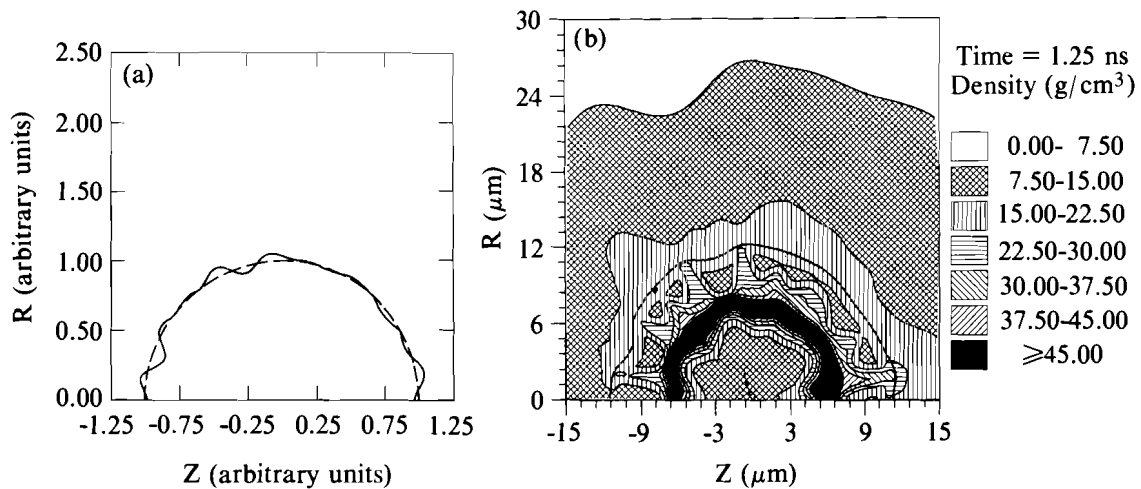
TC2551

Fig. 43.10

Two-dimensional (*ORCHID*) hydrodynamic simulation of a 5-μm-glass-ablator cryogenic implosion subjected to illumination nonuniformities in modes $2 \le \ell \le 20$.

(a) Illumination-nonuniformity pattern placed on target (solid lines) modes $2 \le \ell \le 20$ with a total peak-to-valley of ~15%.

(b) Density contours (g/cm^3) at the time when the simulation yield equaled the level of experimental observed yield for similar-ablator-thickness capsules.

The modal analysis modeling, incorporating modes $\ell \le 500$, indicates that the DT layer could be mixed with the ablator material and very early in the implosion. Because the mixing is predicted to take place early in the implosion, several 1-D pre-mixed simulations were conducted to examine the potential consequences of this mixing on pellet performance. The premixed simulations assume that initially a certain fraction of the inner glass-ablator material is uniformly distributed into the DT fuel.

Figure 43.11 shows the measured neutron yields and the 1-D results of the premixed simulations for several SiO$_2$-to-DT mix ratios. The results for the measured and calculated neutron-weighted fuel areal density are shown in Fig. 43.12. The yield results (see Fig. 43.11) show that the mixing of ablator material with the DT during the acceleration phase of the implosion has a large influence on the neutron yield. These simulations do not take into account energy associated with mixing during the stagnation phase and neglect the effects of the other sources of potential departure from one-dimensional behavior discussed previously. For example, 2-D simulations of the effects of long-wavelength modes on the premixed implosions show additional yield reductions of 2 to 10, depending on the illumination-nonuniformity level. Therefore, combining the dominant effect of acceleration mixing of DT and ablator with long-wavelength-modes effects,
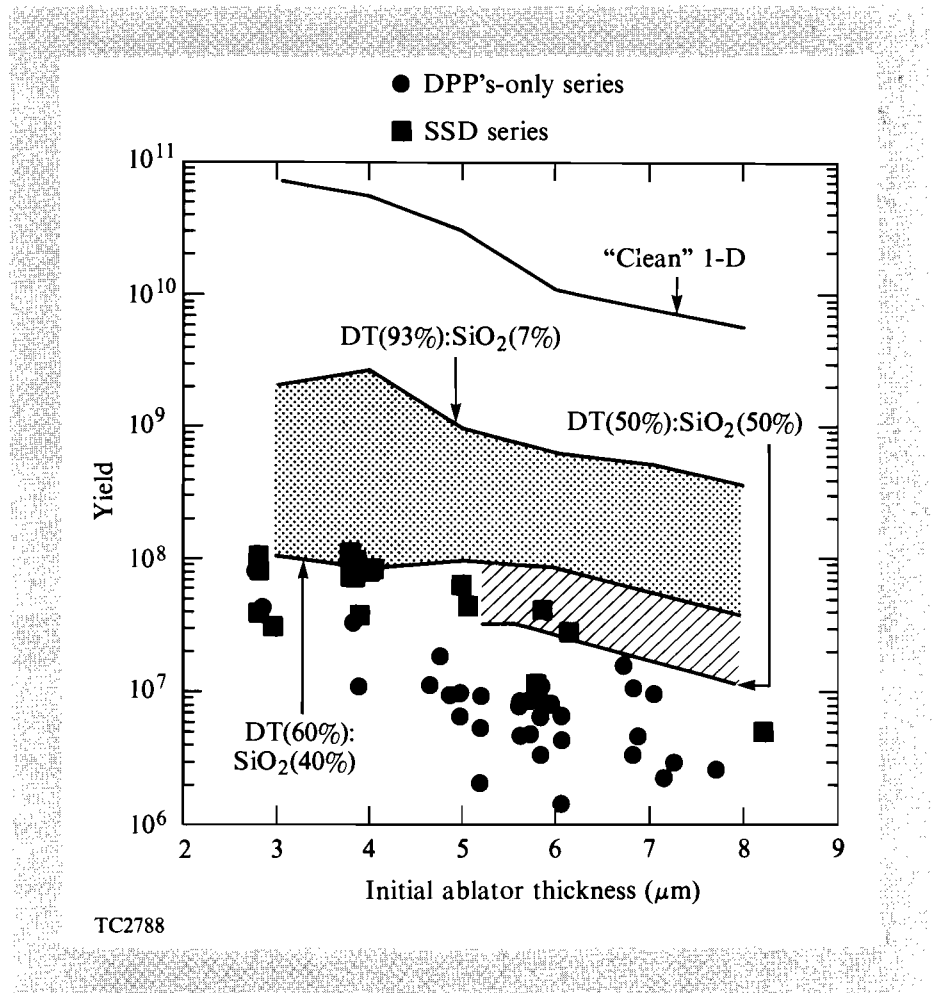
Fig. 43.11
Observed yields and one-dimensional hydrodynamic simulation yields assuming a number of DT-to-SiO₂ fuel (pre-mixed) mix ratios versus initial ablator thickness.

results in yields consistent with those observed in the experiments. Figure 43.12 shows that the predicted fuel areal densities from the premixed simulations bracket the values of ρR_f observed experimentally.

Of course, these mix estimates are *ad hoc*. Currently it is impossible to define a unique level of mixing that must have taken place during these implosions. A detailed knowledge of the contributions of long-wavelength modes and the source and levels of perturbations at the unstable regions would be required for such a calculation. We have assumed that the perturbations at the fuel-ablator interface region were the result of feed-through of drive nonuniformities from the ablation surface. However, the inside-surface finish of the glass targets and potential early nonuniform "freeze out" of high-Z contaminants in the DT fuel could also act as initial perturbations at the DT-ablator interface. These sources of initial perturbations can vary from capsule to capsule. However, assuming mixing

● DPP's-only series

■ SSD series

TC2789
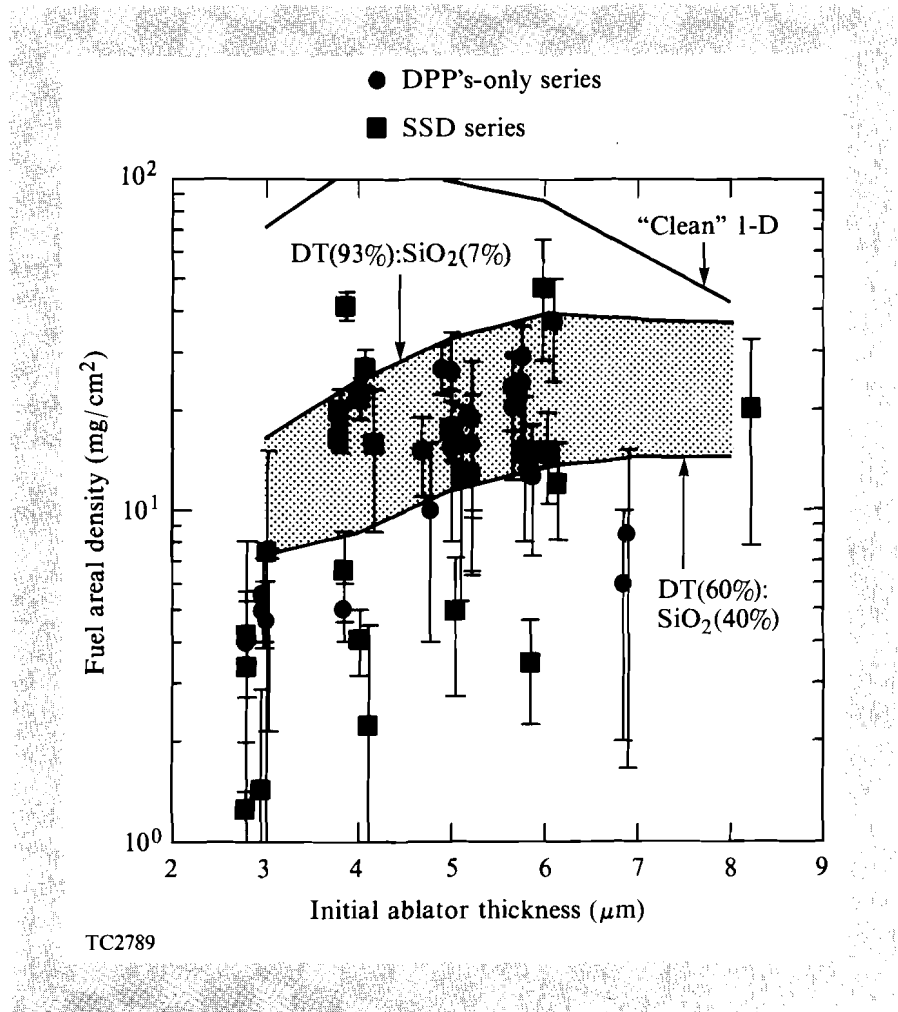
Fig. 43.12
Measured fuel areal densities and one-dimensional predicted fuel areal densities
assuming a number of DT-to-SiO$_2$ fuel (pre-mixed) mix ratios versus initial ablator
thickness.

ratios higher than about 50% DT:50% SiO$_2$ does not appear plausable
because the predicted fuel areal density would be much lower than that
observed experimentally (see Fig. 43.12).

This study has identified that the classically unstable interface within the
DT, and subsequent mixing with ablator material during the acceleration
phase, could be the dominant contributor to the observed departures
between glass-ablator cryogenic-implosion experimental results and
simulation predictions. (Unstable flow development in the ablator becomes
increasingly important as the initial ablator thickness increases.) The
classical Rayleigh-Taylor growth rates, in conjunction with the thinness
(≤5 μm) of the cryogenic fuel layer during the acceleration phase, place
severe constraints on required levels of illumination uniformity and the
finish of the fuel-glass interface.

Proposed high-gain direct-drive capsule designs have been planned to eliminate the occurrence of a classical growth Rayleigh-Taylor unstable region in the fuel layer near the ablator-fuel interface by using low-atomic-number ablators and pulse shaping. Experiments planned for OMEGA will begin to address the hydrodynamic behavior of capsules more closely related to the proposed high-gain designs. This study will be carried out in three broad stages. The first stage will examine the hydrodynamic behavior during the acceleration phase of low-atomic-number ablator capsules. The second stage will use noncryogenic "surrogate" cryogenic capsules to examine the dynamics of a hydrodynamically equivalent, surrogate cryogenic capsule implosion. Finally, upon successful completion of the first two stages, cryogenic-capsule implosions using low-atomic-number ablators will be conducted. This phase in the experiments will require advances in target-fabrication techniques since the initial fuel-layer thickness will be of the order of 20 to 30 μm.

ACKNOWLEDGMENT

REFERENCES

1. F. J. Marshall, S. A. Letzring, C. P. Verdon, S. Skupsky, R. L. Keck, J. P. Knauer, R. L. Kremens, D. K. Bradley, T. Kessler, J. Delettrez, H. Kim, J. M. Soures, and R. L. McCrory, *Phys. Rev. A* **40**, 2547 (1989).

2. R. L. McCrory, J. M. Soures, C. P. Verdon, F. J. Marshall, S. A. Letzring, S. Skupsky, T. J. Kessler, R. L. Kremens, J. P. Knauer, H. Kim, J. Delettrez, R. L. Keck, and D. K. Bradley, *Nature* **335**, 225 (1988).

3. G. Taylor, *Proc. R. Soc. London Ser. A* **201**, 192 (1950).

4. D. J. Lewis, *Proc. R. Soc. London Ser. A* **202**, 81 (1950).

5. S. Chandrasekhar, *Hydrodynamic and Hydromagnetic Stability* (Clarendon Press, Oxford, England, 1961), Chap. 10.

6. LLE Review **33**, 1 (1987).

7. S. Skupsky, R. W. Short, T. Kessler, R. S. Craxton, S. Letzring, and J. M. Soures, *J. Appl. Phys.* **66**, 3456 (1989).

8. B. I. Bennett, J. D. Johnson, G. I. Kerley, and G. T. Rood, Los Alamos National Laboratory Report LA-7130 (1978).

9. W. F. Huebner, A. L. Merts, N. H. Magee, Jr., and M. F. Argo, Los Alamos National Laboratory Report LA-6760-M (1977).

10. M. Born and E. Wolf, *Principles of Optics* (Pergamon, New York, 1975), p. 123.

11. R. C. Malone, R. L. McCrory, and R. L. Morse, *Phys. Rev. Lett.* **34**, 721 (1975).

12. P. C. Souers, *Hydrogen Properties for Fusion Energy* (University of California Press, Berkeley, CA, 1986).

13. S. Skupsky and S. Kacenjar, *J. Appl. Phys.* **52**, 2608 (1981).

14. S. Kacenjar, S. Skupsky, A. Entenberg, L. Goldman, and M. Richardson, *Phys. Rev. Lett.* **49**, 463 (1982).

15. S. Kacenjar, L. M. Goldman, A. Entenberg, and S. Skupsky, *J. Appl. Phys.* **56**, 2027 (1984).

16. LLE Review **31**, 101 (1987).

17. J. D. Kilkenny *et al.*, *Rev. Sci. Instrum.* **59**, 1793 (1988).

18. D. K. Bradley, J. Delettrez, P. A. Jaanimagi, F. J. Marshall, C. P. Verdon, J. D. Kilkenny, and P. Bell, in *High Speed Photography and Videography and Photonics VI*, Vol. 981 (SPIE, Bellingham, WA, 1988), p. 176.

19. LLE Review **37**, 16 (1988).

20. R. Lelevien, G. J. Lasher, and F. Bjonklund, Lawrence Livermore National Laboratory Report No. UCRL-4457 (1955).

21. S. W. Haan, *Phys. Rev. A* **39**, 5812 (1989).

1.B   Analysis of Neutron Time-of-Flight Data

The fuel-ion temperature can be determined from the neutron-energy spectrum obtained with a neutron time-of-flight (TOF) detector.[1] For present target conditions, the energy spectra of neutrons produced in deuterium-tritium (DT) and pure deuterium (DD) fuel implosions are unaltered by the outer target layers and, therefore, contain valuable information about the temperature of the reactants in the core region. LLE has successfully deployed several neutron TOF spectrometers.[2] A method has been developed to unfold the neutron-energy spectrum from the observed signal and extract the fuel-ion temperature. This method is verified by modeling the TOF detector and the fuel with Monte Carlo techniques. The Monte Carlo model provides a method of statistical error analysis that yields information on the number of detected events required to extract a useful fuel-ion temperature from ICF neutron TOF data.

Method of Analysis

During an ICF implosion, fuel ions acquire a thermal energy distribution, which causes the neutron energy spectra to be Doppler broadened. The relationship between the fuel-ion temperature and the broadening of the neutron energy spectrum was derived by Brysk,[3] using the following assumptions: the ion thermal velocity distribution is Maxwellian; there is negligible nonthermal ion motion; and the fusion cross section has a form predicted by semiclassical Gamow theory.[4] These derivations showed that the neutron energy spectrum is Gaussian with the full-width at half-maximum (FWHM), ΔE, proportional to the square root of the ion temperature t_i:

$$\Delta E = 177 * \sqrt{t_i}, \tag{1}$$

$$\Delta E = 82.5 * \sqrt{t_i} \tag{2}$$

for DT fuel and DD fuel, respectively.

The detected signal consists of a convolution of the detector-response function, the neutron temporal-emission history, and the thermally broadened neutron spectrum. In our present target experiments, the neutron-emission pulse width is of the order of ~150 ps, which is significantly less than the instrument's 600- to 800-ps response time.

Analysis of the observed neutron TOF signal thus amounts to deconvolution of the detector-response function from the thermally broadened neutron-energy spectrum. Since applying deconvolution to a noisy signal can be numerically troublesome, we have developed a convolution-fitting program, CONGAUSS, which uses an averaged, measured, detector-response function and a neutron spectrum determined from a fuel model, to unfold the TOF spectrum. We currently model the fuel with a Gaussian neutron-energy spectrum based on Brysk's results.

For a range of temperatures, the model Gaussian neutron-energy spectra are convolved with the detector-response function to create a table containing the ion temperature represented by the Gaussian and the FWHM of the corresponding convolved function. A search is made through this table, looking for the convolved function that has the minimum $\chi^{(2)}$ with the observed data. The appropriate fuel-ion temperature is then extracted from the table.

Results of Analysis: Experimental

Two neutron TOF detectors are used for ICF experiments on OMEGA, one at 10 m for DT targets and the other at 1.8 m for DD targets. The detectors consist of a 1%-quenched Bicron BC-422 scintillator, 3.81 cm in diameter and 2.54 cm thick, optically coupled to ITT F4129f microchannel-plate photomultiplier tubes. These detectors have calculated neutron-detection efficiencies of about 6%. The electronic signal from the photomultiplier is recorded on a Textronix 7104 oscilloscope equipped

with a 7A29 plug-in, which provides 1-GHz bandwidth. The oscillograph from this recording system is digitized using an inexpensive hand scanner and personal computer.

Figure 43.13 shows the averaged detector response to random cosmic rays for the 10-m neutron TOF detector. This signal represents an average over ten detected events. The response function has a FWHM of 0.8 ns and contains an electronic artifact in the pulse tail.

Figure 43.14 shows data from a DT target and the convolved function from which the energy spectrum FWHM was derived. On this experiment, approximately 400 events were detected in the 10-m TOF detector. The analysis, using CONGAUSS, yielded a fuel-ion temperature of 2.3 keV. The pulse height of the convolved function has been normalized to that of the data to do the $\chi^{(2)}$ calculation.

Results of Analysis: Monte-Carlo Modeling

To check the accuracy of our data reduction and to model the fundamental physics of the neutron-detection process, a Monte Carlo simulation was
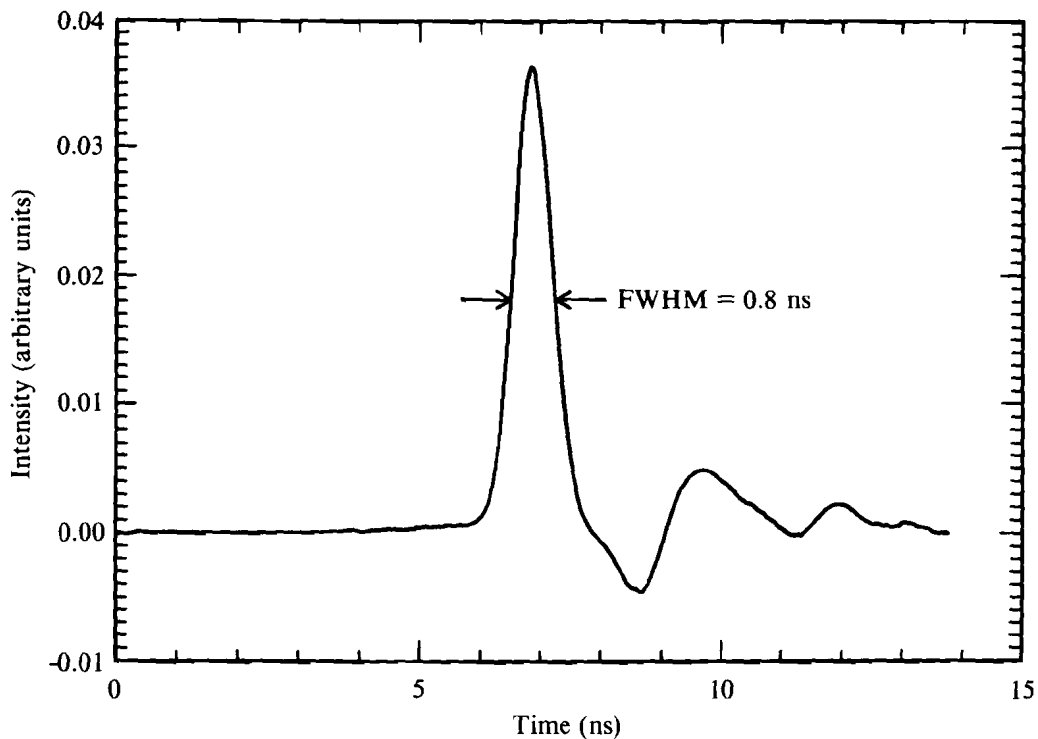
E5411

Fig. 43.13
Averaged detector-response function of the neutron time-of-flight detector located 10 m from the target.

E5523
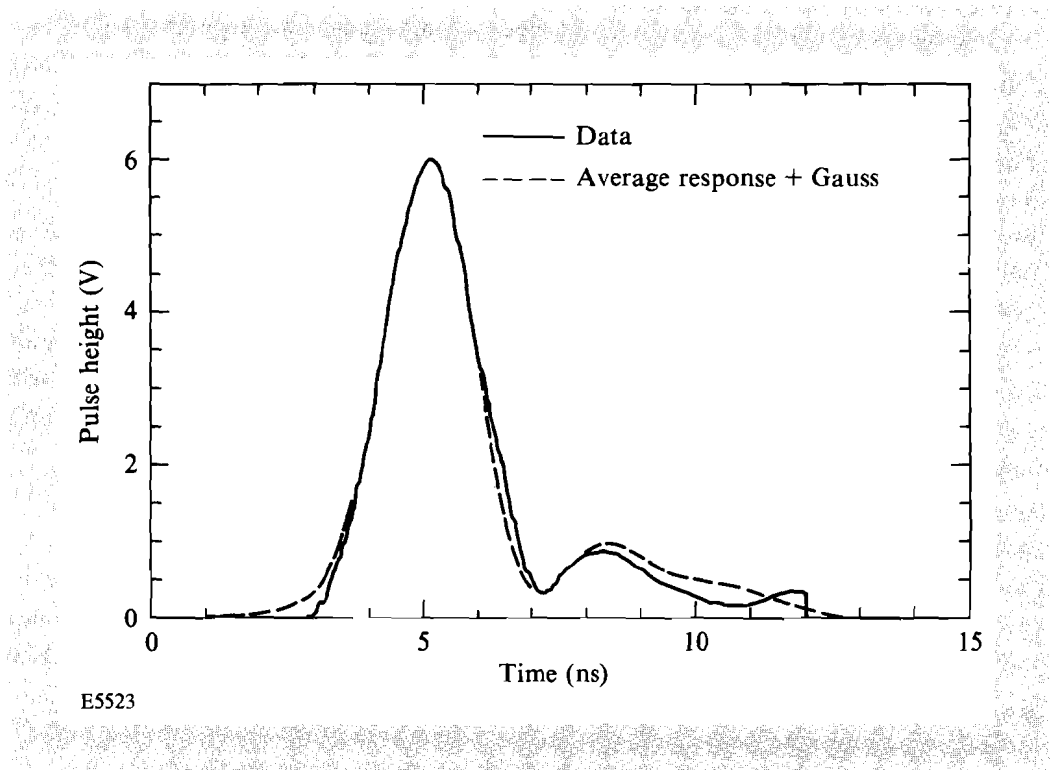
Fig. 43.14
Comparison of neutron TOF data and the convolution of the detector-response
function and time-converted Gaussian energy spectrum from which an ion
temperature of 2.3 ± 0.8 keV is extracted. A $\chi^{(2)}$ of 0.054 was calculated for this fit.
This was shot number 16176 for which there were 400 detector hits.

performed. The model for this simulation uses the measured, single-
neutron electronic response of the detector to simulate the shape of each
neutron event and theoretical probability functions to simulate the pulse
height of the detector and neutron times-of-arrival. Neutrons interact by
colliding with protons in the plastic (hydrogenous) scintillator. The proton
recoil produces a light flash, which is detected by a photomultiplier. The
model for the observed pulse-height distribution uses two assumptions:
a uniform proton-recoil spectrum and a light output L from the proton-
detection process with the following functional form[5]:

$$L \sim E^{1/3} ,$$

where E is the proton-recoil energy. The cumulative probability distribution
for the pulse height H' is

$$P(H') = H'^{2/3}/H'_{max}^{2/3} ,$$

where H'_{max} is the pulse height at maximum recoil energy. Note that the
pulse heights will vary from 0 to H'_{max}, which is typically around 0.1 V.
These pulse-height variations cause uncertainty in the number of detected
events. To simulate the time of arrival of each neutron we used a Gaussian

energy distribution. However, the program is not restricted to this fuel model, thus allowing more complex fuel conditions to be modeled at a later time.

The input parameters to the simulation are the ion temperature and the number of detected events. The shape of each detected event is represented by the detector-response function, while the pulse height and time of arrival are obtained from respective cumulative probability distributions. The time- and height-adjusted response functions are then summed to obtain the resulting (current-mode) time-of-flight spectrum. Figure 43.15 shows a comparison of the neutron TOF data analyzed earlier and a Monte Carlo simulation with the same parameters. The simulation is in good agreement with the data. The Monte Carlo simulation routine was tested by extracting the ion temperature of the simulated detector signal using the reduction program CONGAUSS. The result is shown in Fig. 43.16. For a model input temperature of 2.3 keV, CONGAUSS extracts an ion temperature of 2.5 keV, which is within the statistical error of the simulation. Repeating the simulation several times with an ion temperature of 2.3 keV and 400 detected events, we consistently see uniformly shaped simulated pulses from which we can extract reasonable ion temperatures. However, when the number of detected events is significantly less, the simulations show wildly varying pulse shapes from which a fuel-ion temperature cannot be extracted without large errors. This suggests that there is a minimum number of detected events required to create a TOF spectrum that will yield a credible ion temperature. To investigate this point further, we have done a statistical error analysis using the Monte Carlo program.

Fig. 43.15
Monte Carlo simulation of TOF data with a 2.3-keV ion temperature and 400 detected events. The data simulated is from shot number 16176; $\chi^{(2)}$ of the fit is 0.061.

E5521

E5522
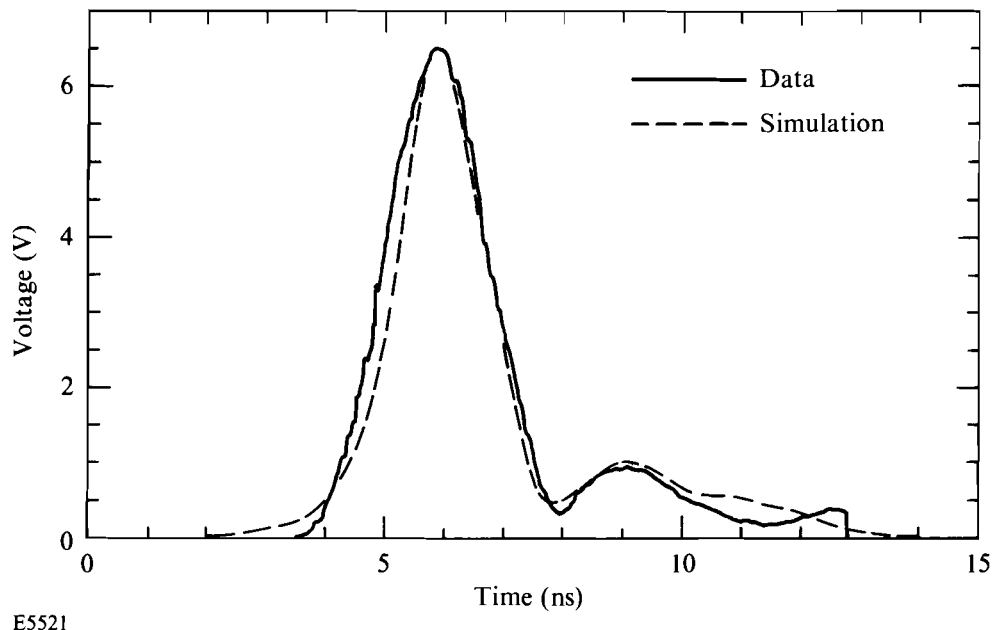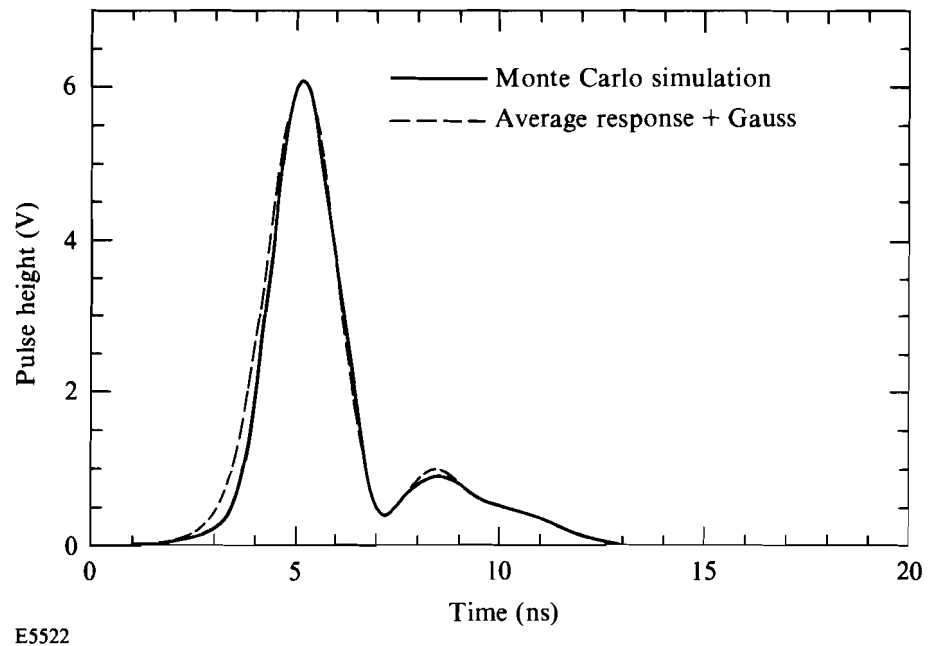
Fig. 43.16
Comparison of Monte Carlo simulation with the convolved function from
CONGAUSS. The simulation temperature is 2.3 keV and the ion temperature
extracted from CONGAUSS is 2.5±1.0 keV. 400 detected events were used in the
simulation; the comparison gives a $\chi^{(2)}$ of 0.025.

For a given ion temperature the simulation was executed 200 times using various numbers of detected events at a single ion temperature. Each simulated pulse was used as input to CONGAUSS, which extracted the ion temperature of the TOF spectrum. In Fig. 43.17 the fractional error in the ion-temperature measurements generated from the Monte Carlo routine is compared with the theoretical,

$$2 / \sqrt{2N},$$

fractional error.[6] The difference between the curves reflects the error incurred by not knowing the exact number of detected events. As expected, the fractional error in ion temperature declines with increasing numbers of detected events. However, the absolute error, and thus the fractional error, depends on the ion temperature as well. As the ion temperature increases for a fixed number of detected events, the spectral energy-density profile becomes broader, thereby creating a larger error. To obtain equal fractional errors for different ion temperatures, a larger number of detected events is thus required for the higher-ion-temperature implosion than the lower-ion-temperature implosion.
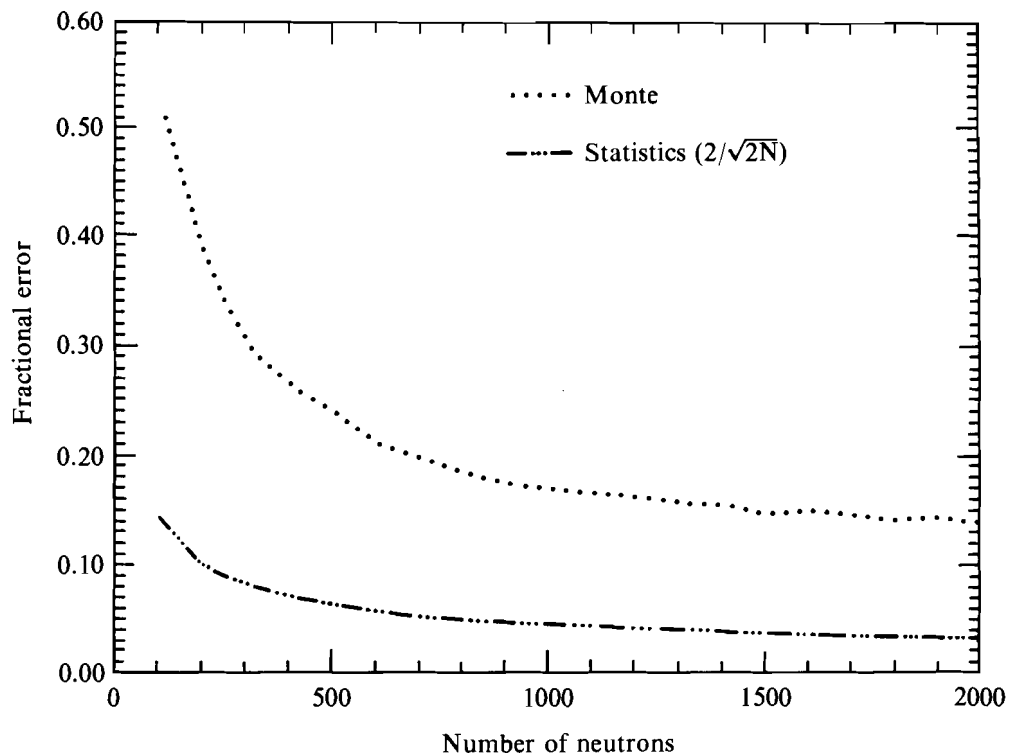
E5626

Fig. 43.17
Plot of fractional error in the fuel ion temperature versus the number of detected neutrons for theoretical statistics and the Monte Carlo calculations using an ion temperature of 2.31 keV.

In our present 1- to 3-keV temperature regime, systematic measurement errors are about 35%. From Fig. 43.17 our error analysis shows a similar error for about 250 detected events. Thus, we require significantly more than 250 detected events to extract a meaningful fuel-ion temperature corresponding to neutron yields $> 4 \times 10^9$ for DT targets on the 10-m TOF detector.

Conclusion

We have developed a method to extract the fuel-ion temperature from ICF neutron time-of-flight data. A useful temperature can be extracted from the data only if a statistically significant number of neutrons are detected. In our present temperature regime, using a single, current-mode detector, accurate measurements of fusion neutron spectra can only be obtained on experiments producing greater than 250 detected events.

REFERENCES

1. R. A. Lerche *et al.*, *Appl. Phys. Lett.* **31**, 645 (1977).

2. LLE Review **27**, 103 (1986).

3. H. Brysk, *Plasma Physics* **15**, 611 (1973).

4. F. Rasetti, *Elements of Nuclear Physics* (Prentice Hall, New York, 1936).

5. G. F. Knoll, *Radiation Detection and Measurement* (John Wiley and Sons, New York, 1979).

6. W. R. Leo, *Techniques for Nuclear and Particle Physics Experiments* (Springer-Verlag, Berlin, 1987), p. 90.

1.C   Precise Control of the OMEGA Laser

The current experiments relevant to the demonstration of inertial confinement fusion require that the target driver be capable of precise control. To control the driver, diagnostics are needed to measure its performance. The OMEGA laser has been through a series of improvements allowing the system to be configured for a specific series of target experiments. These techniques give a well-characterized and reproducible illumination pattern to an implosion target.

OMEGA Energy Balance

The beam-splitting control system on the OMEGA laser has been improved[1] allowing the energy in each of the 24 beams to be balanced with a root-mean-square error of 1%–2%. The primary components of the balance control are computer-controlled wave plates whose rotation is determined by the output of 24 silicon PIN diodes. A schematic of the control system is shown in Fig. 43.18.

The splitter wave plates on OMEGA are now motorized and can be positioned by a PDP-11 minicomputer. The motor controllers are linked together by a parallel signal cable from the computer interface. Each wave plate has a unique address on the bus and as such can be addressed separately. During a beam-balancing sequence, the minicomputer determines the needed setting of the individual wave plates and then sequentially sets the rotation until the desired system split is achieved.
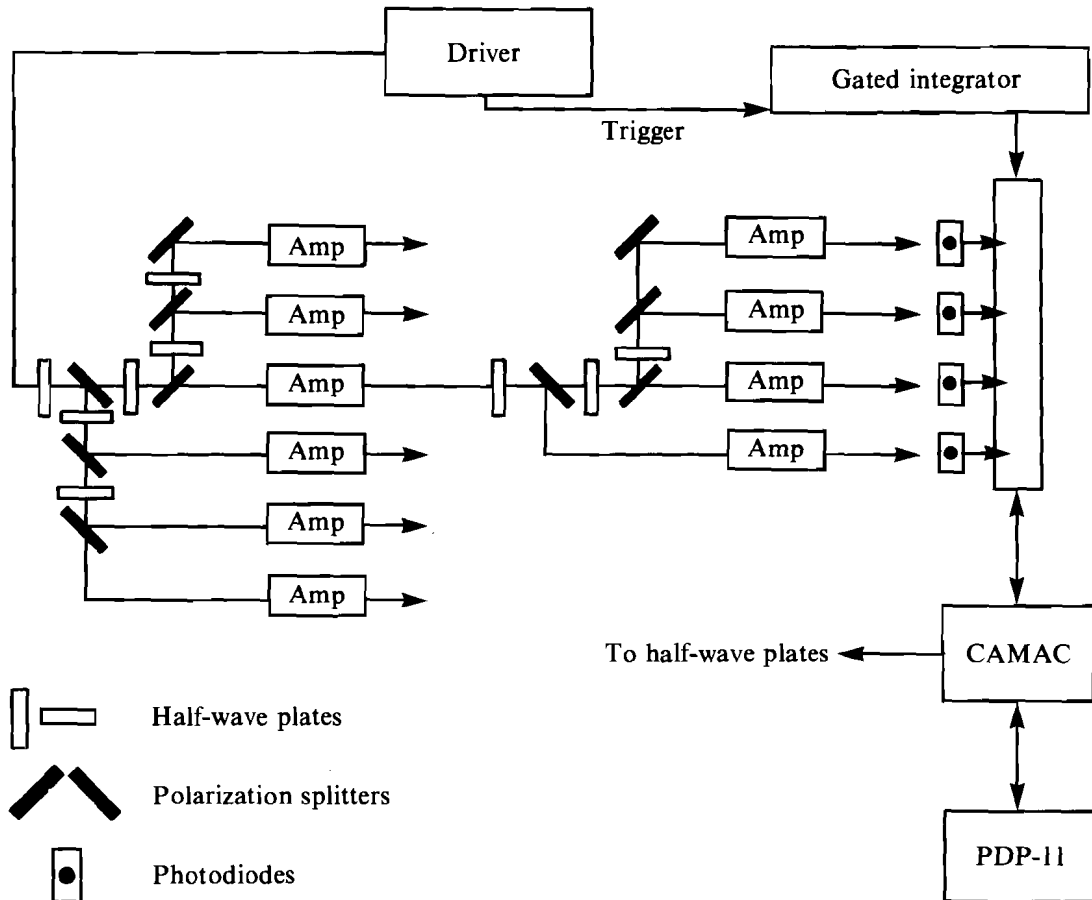
Fig. 43.18
The OMEGA automatic beam-energy-balance system. This system consists of a set of computer-controlled half-wave plates whose rotation is determined by the output of silicon PIN photodiodes.

There are 24 silicon PIN diodes used to determine the rotation angle for the wave plates. These diodes have a Fresnel lens at the input that couples the inner 60% of the beam area to the detector. The detectors are designed to be sensitive to the main OMEGA oscillator, which does not need to be amplified. This allows the laser system to be balanced with a 1-Hz repetition rate. The energy, as reported by on-line calorimetry from previous full system shots, is used as a reference and the minicomputer adjusts the wave plates for the required PIN-diode signal levels.

By using the oscillator, PIN diodes, and motorized wave-plate controllers, the OMEGA laser can have its energy split set during a 1/2-h shot cycle. This procedure can be used to either balance the laser beams or set up a specific energy distribution. The effects of low-order nonuniformity of

laser illumination during a direct-drive target implosion can be determined by inducing a known energy distribution on the OMEGA laser. A reference table on individual beam energies can be used to set the wave-plate rotation for the desired illumination distribution.[2]

Due to these improvements in the energy-distribution control, OMEGA can now be used for a series of experiments that were not possible previously. The overall system-energy-balance error has been improved from 3%–5% to 1%–2%. All this can be accomplished within a single shot cycle so that, as conditions change during a shot series, the laser-system energy settings can be reestablished to the experimental requirements.

Small-Signal-Gain Measurements

The silicon diodes that are used for the energy balancing of OMEGA have been used to measure the small signal gain of each amplifier. This allows system performance to be monitored and maintenance tasks assigned when an individual amplifier is outside its performance specifications. The importance of gain control to power balance was discussed in an earlier LLE Review.[3] By using the main OMEGA oscillator and a series of calibrated neutral-density filters, it is possible to measure the gain of all amplifiers in a day. A reference diode is used to monitor the oscillator output, and the 24 energy-balance diodes are used to measure the amplified oscillator pulse. The lens used in front of the balancing diodes samples a large enough portion of the laser beam to accurately determine the amplifier gain.

It is possible to match the beamline gains by changing amplifier rods after a small-signal-gain measurement.

OMEGA Target-Integrating Sphere

To be used for experiments, the laser output must be transported to the target. The OMEGA transport system uses three to four mirrors, a distributed phase plate (DPP), a focus lens, and a blast shield/vacuum window for each beam. The reflection of each mirror and the transmission of the DPP, lens, and blast shield for all beams must be measured and monitored. The technique currently employed on OMEGA uses a small integrating sphere at the center of the target chamber to measure the UV transport efficiency.

A schematic of the measurement configuration is shown in Fig. 43.19. The output from an argon-ion laser is tuned to 351 nm and is injected into an OMEGA beam after the frequency-conversion crystals. A portion of this beam is split off into an integrating sphere as a reference. The beam is then transported to the target chamber where a second integrating sphere measures the beam energy. The ratio of the signals from these two detectors determines the transport efficiency of the beamline. The argon-ion laser beam is chopped so that a stable, high-gain, lock-in amplifier can be used to measure the energy in the transported beam.
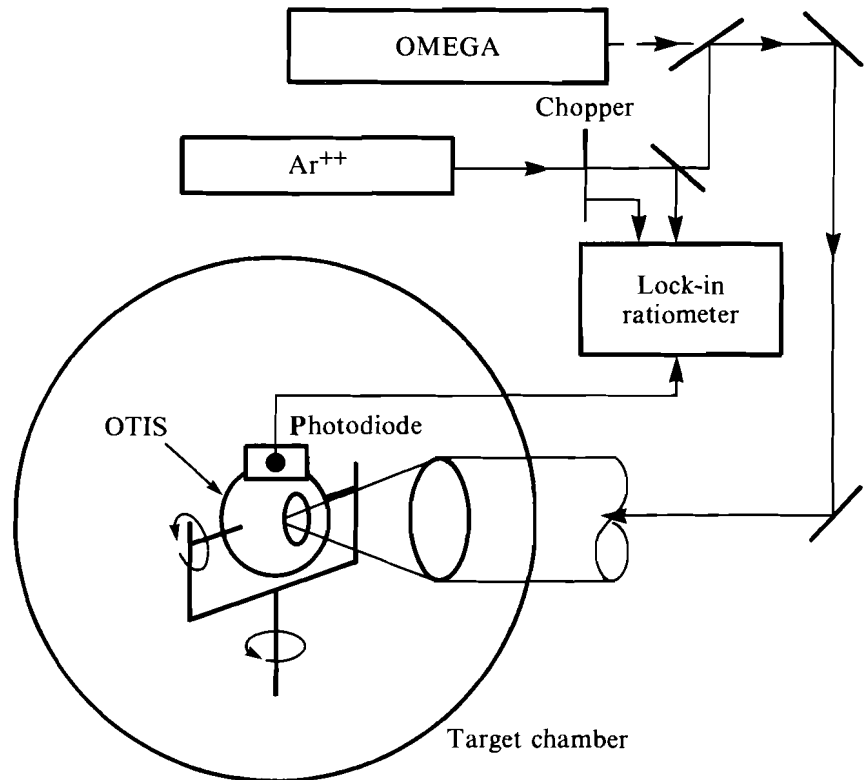
Fig. 43.19
The OMEGA transport integrating-sphere system (OTIS). An Ar^{++} ion laser is injected into an OMEGA beamline after the frequency-conversion crystals. The signal as measured at the center of the target chamber is ratioed with a reference signal to measure the transport efficiency.

The target-integrating sphere is small enough to be inserted into the target chamber without removing target diagnostics. A two-axis angular control allows the input of the sphere to be directed to each of the OMEGA beam ports. Thus, it is possible to measure the transport efficiency of all 24 beamlines in 4 h with a 1%–2% accuracy. The transport measurement is now scheduled as a routine target-chamber maintenance task with minimum impact on system operation.

Pointing with X Rays

The final pointing of the OMEGA beams is done by measuring the beam position with a gold-coated target, which is 800 μm in diameter with a 1-μm-thick gold coating. The x rays emitted by this target are measured with six reentrant pinhole cameras distributed around the OMEGA target chamber so that the position of all 24 beams can be determined. The cameras are tuned to the gold N- and M-shell x-ray emission. The 1-μm-thick Au layer is about three times the thickness that would be burned

145

through by an OMEGA beam. This ensures that all beams are measured equally and that the layer thickness does not affect the x-ray image.

After a system shot the images are processed and digitized with a video digitizer connected to a solid-state camera, which is interfaced to a microscope with a magnification of 3. This same system is used for the measurement of "knock-on" data from an OMEGA implosion target.[4] An image from a pointing shot is shown in Fig. 43.20. The x-ray image shown in Fig. 43.20(a) is taken before the system pointing has been corrected. The root-mean-square pointing error is 18 μm with the worst beam mispointed by 31 μm. A table of corrections for the positions of each targeting mirror is generated and used to repoint the beams. Figure 43.20(b) shows an image after this correction has been made. The rms pointing error is now 10 μm and the worst error is 22 μm. These errors are measured on the surface of the 800-μm-diam pointing target. This procedure is repeated until the rms pointing error is less than 10 μm and the worst beam is displaced less than 20 μm from its optimum position. The time between pointing shots is about 1 to 1.5 h and includes the time needed for film processing, digitization, measurement, and mirror correction of 24 beams. A full shot day is allocated to point the system when it is initially started at the beginning of a shot week. Pointing is checked at the start of each shot day, when only small corrections are needed.

(a) Shot 19457   (b) Shot 19461

σ_{rms} = 18 μm σ_{rms} = 10 μm
Worst = 31 μm   Worst = 22 μm
Median = 15 μm   Median = 7 μm
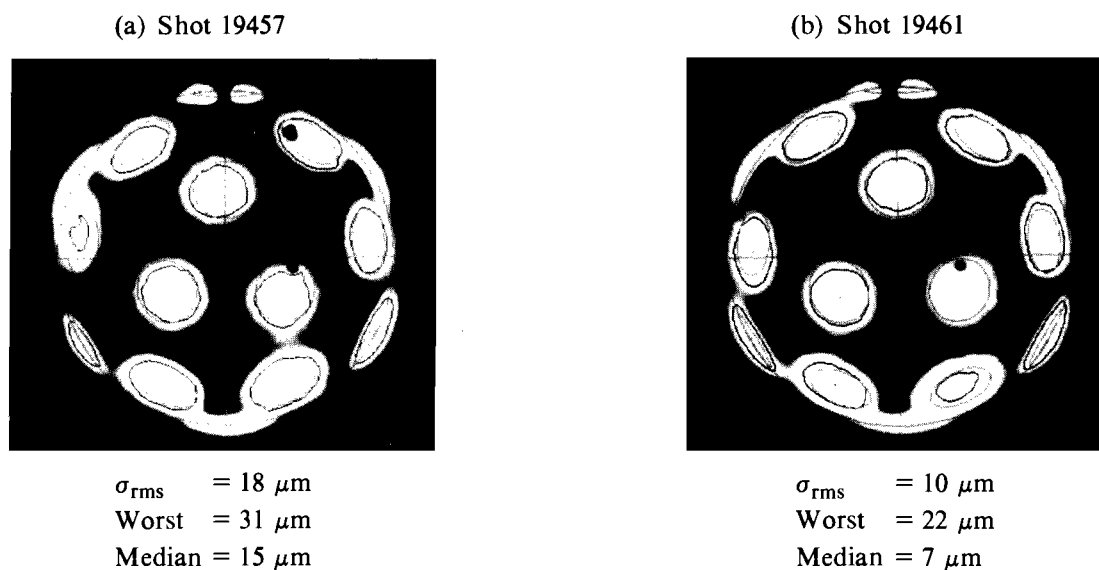
E5383

Fig. 43.20
Final laser pointing using x-ray images. The x-ray emission from Au-coated targets is used to measure the position of each beam on a sphere. This image is used to arrive at a set of corrections for the position of each targeting mirror.

Target Drive Uniformity

The illumination uniformity of the laser is checked by measuring the x-ray emission from a small implosion scale target. This target is 250 μm in diameter with a 1-μm-thick layer of gold coated on the outside. The 250-μm diameter is matched to the diameter of the OMEGA implosion targets and as such serves as a good measure of the drive conditions. The x rays are measured with both the reentrant pinhole cameras and the Kirkpatrick-Baez microscopes. The images are then digitized with a photographic digitizer interfaced to a SUN workstation.

Uniformity images are shown in Fig. 43.21. Figure 43.21(a) shows an image taken before all improvements in the OMEGA controls were implemented. The energy was balanced to ±8.9% rms and is an example of very poor drive uniformity. The projected image is a sinusoidal projection that preserves the area on the sphere. It is evident that there are 100% peak-to-valley intensity variations in the laser illumination. An example of a ±4.7%-rms-energy-balanced laser system is shown in Fig. 43.21(b). The improved uniformity is apparent in the projected image. The peak-to-valley variations are about 20%. A sinusoidal projection is made from three

Fig. 43.21

A record of illumination uniformity is taken with an x-ray image of a target having the same diameter as an implosion target. At least two individual images are used to arrive at a sinusoidal projection of the intensity distribution for the entire target.

(a) Example of poor uniformity (energy imbalance ±8.9%)

Distance (μm)

(b) Example of improved uniformity (energy imbalance ±4.7%)

Distance (μm)

Single x-ray image

Computed irradiation distribution

E5382

147

individual camera images. An example of a single image is shown adjacent to the projected images. These targets allow the drive conditions to be monitored on each shot day.

Summary

Improvements to both laser control and diagnostics have allowed the OMEGA laser to be used with greater precision than previously possible. The automatic splitting of the OMEGA beams is essential in the setup and stability of the system. The current energy balance of 1%–2% is well characterized at the output of the frequency-conversion cells. The energy is then transported to the target using transport optics that are characterized to 1%–2% with an integrating sphere inside the target chamber. This gives an overall system-energy balance of 1.5%–3% rms. The final laser pointing uses x-ray images to optimize the system for target shots. The illumination uniformity for each shot day is characterized using an x-ray-emitting target that is the same size as an implosion target. All of these techniques are essential to perform the relevant target experiments to demonstrate the capabilities of inertial confinement fusion.

ACKNOWLEDGMENT

REFERENCES

1. LLE Review **37**, 25 (1988).

2. P. W. McKenty, S. Skupsky, D. K. Bradley, W. Seka, and C. P. Verdon, "Numerical Determination of the Effects of Laser Power Balance on the Levels of Illumination Nonuniformities," presented at the APS Division of Plasma Physics Meeting, Anaheim, CA (1989).

3. LLE Review **41**, 1 (1989).

4. LLE Review **36**, 148 (1988).

Section 2

ADVANCED TECHNOLOGY
DEVELOPMENTS

2.A Transparent Conductive Coating of KDP Using Ion-Assisted Deposition

Several types of electro-optic devices require electrodes that are both optically transparent and electrically conductive. Examples of such devices useful for inertial fusion lasers are given in Table 43.I. Some devices, such as the longitudinal Pockels cell, require application of a transparent electrode to a thermally sensitive substrate of potassium dihydrogen phosphate (KDP). The applied coating must also have a high laser-damage threshold for the infrared (1054 nm). A variety of methods[1] have been developed for depositing transparent conductors, but most require heating the substrate to promote complete oxidation of the film. This article describes a technique for depositing transparent conductors using indium-tin oxide (ITO) with ion-assisted deposition (IAD).

Both thin metal films and oxide semiconductors have been used for transparent conductors. Metal films have high absorption, hence, a correspondingly low laser-damage threshold, making them unsuitable for the applications listed in Table 43.I. The high transparency of the oxide-semiconductor films derives from their high band gap energy, i.e., $> 3.0\,\text{eV}$. Optical losses in the films have two origins: (1) interfacial reflection losses caused by refractive index mismatch to the substrate and incident media; and (2) absorption losses caused by non-stoichiometric films or impurities introduced to induce conduction. The first loss mechanism may be compensated for by appropriate optical-thin-film design. The second mechanism must be balanced against the need for low electrical resistance.

Table 43.I: Transparent conductor requirements for devices used in high-energy lasers.

Device	High Transparency	Low Resistance	High Fluence	Thermal Limits
Profile-tunable liquid crystal laser aperture[2]	X			X
Liquid crystal beam steering and switching	X	X		
Longitudinal-mode KDP Pockels cell	X	X	X	X

G2947

In addition, an abundance of free carriers (electrons) in the film can produce a plasma resonance peak in the infrared (for ITO this is about 1.5 μm). At infrared wavelengths longer than this absorption peak the coating will be highly reflective.

The intrinsic conductivity σ of a material is directly related to the carrier density N, carrier mobility μ, and the carrier charge e, such that $\sigma = Ne\mu$. Conduction in oxides may be enhanced by the introduction of free carriers into the lattice. These carriers may originate either from a departure from the stoichiometric oxide or by the introduction of impurity (dopant) atoms into the lattice. In this work we use indium oxide (In_2O_3) doped with tin giving an N-type conductivity. Both the high-valence tin and the oxygen vacancies contribute to conductivity in ITO. Carrier mobility also has a significant effect on conductivity. The mobility in a transparent conductor is impeded by scatter from grain boundaries, ionized impurities, and the interfaces. All of these mechanisms contribute to a low mobility in the thin-film form when compared to the bulk material.

A complex picture forms when the realities of the thin-film process are considered. A change in a single-process parameter, such as substrate temperature, evaporation rate, or oxygen backfill pressure, can simultaneously alter film stoichiometry and structure. Independent control of carrier density and mobility can therefore be very difficult. If temperature control is removed by substrate constraints, it is not possible to obtain stoichiometric films since oxidation is incomplete at the film surface. Ion-assisted deposition (Fig. 43.22) can provide the additional control by bombarding the substrate with relatively high-energy ions (with respect to the low thermal energy of the evaporant). By controlling the ion energy and flux, significant changes in the film structure can be induced.[3,4] If the ion
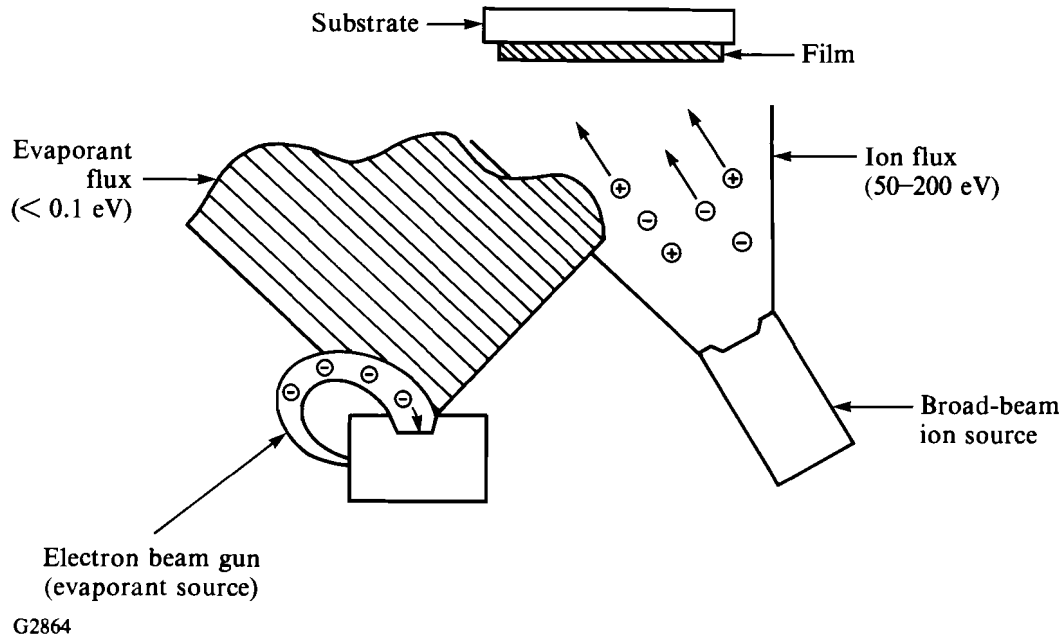
Fig. 43.22
Schematic of ion-assisted deposition. The low-energy evaporant flux is given additional kinetic energy by the high-energy ions at the film formation surface. An inert or reactive gas (such as oxygen) may be used for the ion flux. Oxygen, which was used for the ITO coatings, promotes oxidation at the interface if it is not too energetic.

is a reactive species, such as oxygen, the stoichiometry may also be affected by both implantation and preferential sputtering.

Coatings with high laser-damage thresholds generally must have low absorption at the laser wavelength. However, transparent conductors will have some absorption (due to free carriers), but it can be minimized by increasing conductivity with higher carrier mobility. IAD is used to control the grain size and the stoichiometry while maintaining the substrate at near-ambient temperature. This method is used to coat KDP with a transparent conductor of ITO. Holding the KDP at a temperature close to ambient avoids deleterious effects caused by the differential expansion coefficients of KDP.[5]

Experimental Procedure

1. Deposition-chamber geometry

The ITO coatings were produced in a 28-in.-diam cylindrical vacuum chamber. The chamber contains an electron-beam evaporation source and an 8-cm-aperture broad-beam ion source, which are placed approximately 50 cm and 40 cm below the substrate mount, respectively. The ion source has a dual graphite-accelerator grid that is designed to produce a collimated beam of monoenergetic ions.[6] The impingement rate of the ions is measured

by a negatively biased Faraday cup probe located at the height of the substrate mount. Deposition rate of the evaporant mass was monitored by a resonating quartz crystal sensor. A thermocouple located near the substrate holder monitored the changes in ambient temperature of the chamber during the deposition.

The substrates were rotated to obtain better time-averaged uniformity of both the evaporant and the ion source. The ion source was pointed approximately 6 cm away from the center of the substrate rotation[4] to obtain the optimum uniformity of both quantities.

The chamber is evacuated by a cryogenic pump to pressures less than 4×10^{-6} mBar prior to depositions. Continuous addition of oxygen gas through the ion source raises the chamber pressure to 1×10^{-4} mBar during the evaporation. Deposition rate of the ITO evaporant was fixed at 0.1 nm/s for all experiments, and the substrate rotation was kept at 6.6 rpm. All substrates were precleaned for 2 min with 500-eV Ar$^+$ ions at an impingement rate of ~40 μA/cm^2 prior to the onset of film deposition. This step is employed to remove impurities that can hinder the film-substrate adhesion. Following this step, the ion-source parameters were adjusted for subsequent operation with oxygen gas.

2. Characterization

The conductivity of a thin film is often expressed in terms of sheet resistance R_{sh} with units ohms per square (Ω/sq), which is related to the inherent film resistivity ρ and thickness d by

$$R_{sh} = \frac{\rho}{d} .\tag{1}$$

A four-point square-contact probe, illustrated in Fig. 43.23, is used to measure this quantity. After bringing the probe tips in contact with the film surface, a known amount of current is allowed to flow through two adjacent tips, and the voltage generated across the other two tips is measured. The sheet resistance value is then determined from these two quantities with the equation[7]

$$R_{sh} \approx \frac{2\pi}{ln2}\frac{V}{I} = 9.06\frac{V}{I}.\tag{2}$$

The measurement error introduced by physical deviation of the probe from its square design can be determined by averaging measurements from all parallel combinations of current path and voltage measurement.

Optical transparency of the coatings was measured in the wavelength range from 0.3 μm to 25 μm. Figure 43.24 shows some typical results in the visible and near infrared, while the spectrum for 2.5 μm to 25 μm is seen in Fig. 43.25.

$$R_{sh} = \frac{2\pi}{\ln 2} \frac{V}{I}$$

Conducting surface
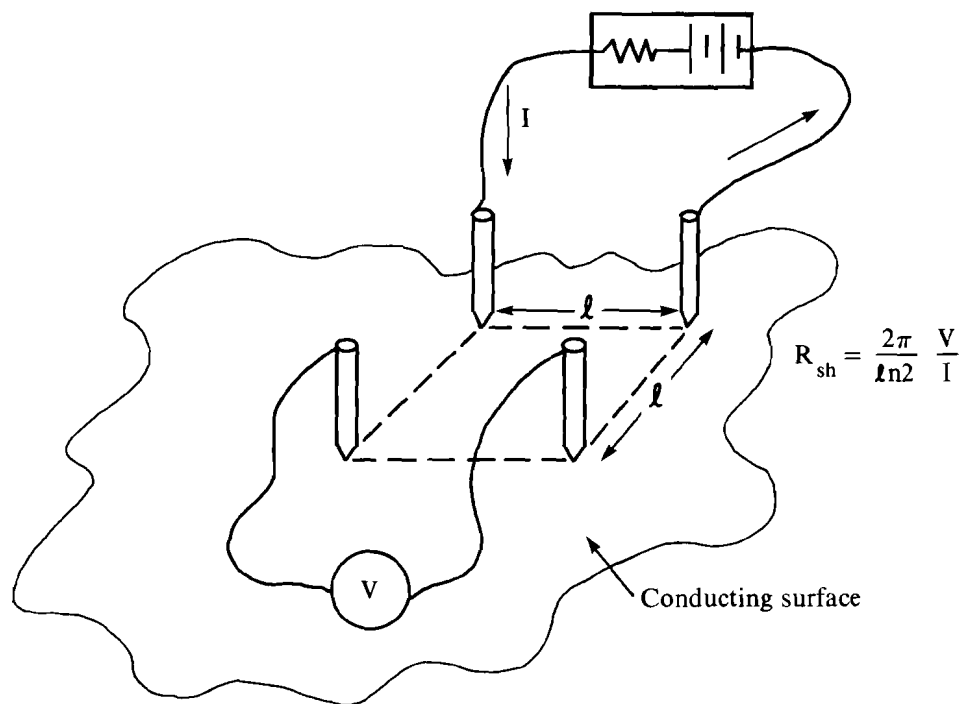
G2936

Fig. 43.23
A four-point square-contact probe apparatus used to measure the sheet resistances of ITO coatings. Only the measurement accuracy is dependent on the size of the square ℓ.

As stated above, the optical and electrical characteristics of transparent conductors are complex functions of numerous quantities (e.g., carrier density and mobility, dopant level, film thickness, and stoichiometry, etc.).[4,7,8] The uniformity of one of these properties across a film surface does not necessarily suggest the uniformity of the other property. Hence, both the optical transparency and the sheet resistance were measured at several locations across the surface of each film sample throughout the experiments.

Results

After adjustment of several process parameters, a reproducible ITO coating with desired transparency and sheet resistance was produced onto a large substrate area. Transparency of the coatings is relatively insensitive to the changes in deposition parameters within the studied range. However, the conductivity, or conversely the resistivity, of ITO coatings is particularly sensitive to the variations in ion energy and flux for a fixed deposition rate.

Controlled variations in the ion energy and flux produce a significant effect on the properties of ITO coatings. Figure 43.26 shows that film

G2937
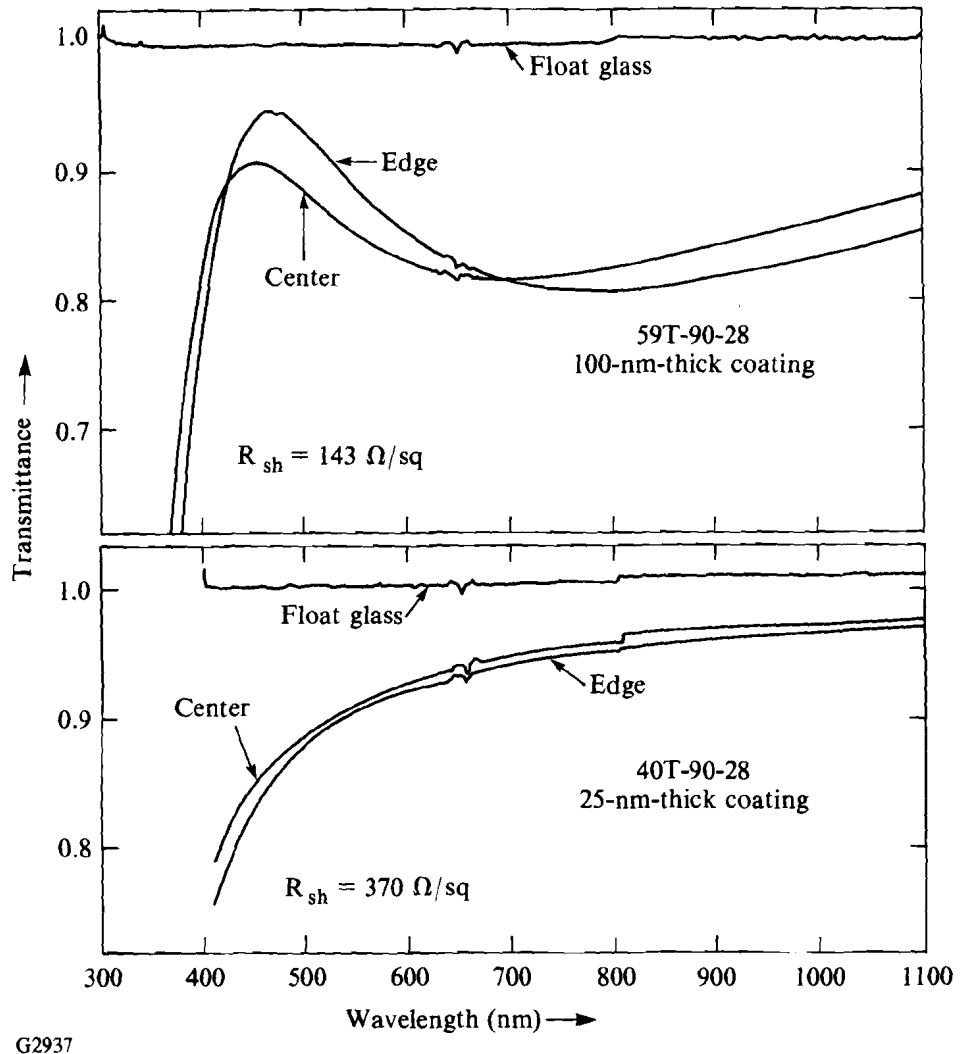
Fig. 43.24
Spectral scans of thick (upper curves) and thin ITO films deposited under optimum IAD conditions at ambient temperatures. The edge pieces were 15 cm from the center of rotation.

resistivity remains at a low constant value for ion energies below 300 eV at a fixed ion-current density. For higher ion energy, a sudden increase in film resistivity occurs. This may have two causes: (1) the film microstructure could be significantly altered, or (2) the higher ion bombardment could produce charge vacancies that act as carrier scatterers. For a fixed ion energy, the resulting film resistivity is particularly sensitive to the ion flux. Figure 43.27 illustrates that < 20% variation in either direction of the optimum ion flux leads to a large increase in film resistivity. From these results, the optimum repeatable ion energy and flux at the substrate for this particular deposition geometry is determined to be 200 eV and 30 μA/cm^2, respectively.
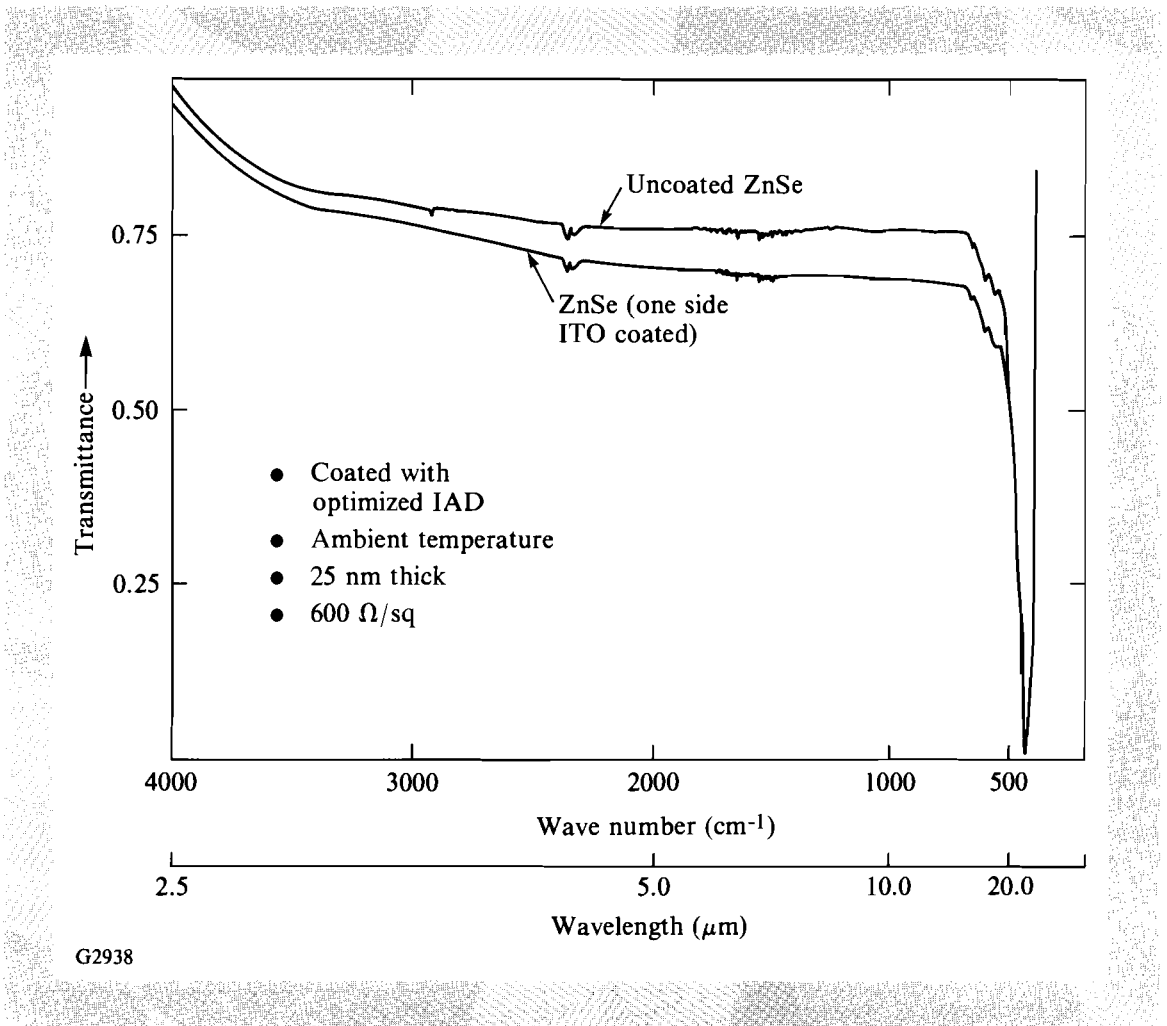
Fig. 43.25
Infrared spectral scan of a thin transparent conductor. The thin coating significantly reduces the strong absorption seen in thicker coatings.

As mentioned in the experimental section, the uniformity of film properties was controlled by varying the ion-source pointing. Figure 43.28 shows that a sheet-resistance uniformity of 12% can ultimately be obtained over a 15-cm diameter after some iterations. The transmission uniformity of films deposited under optimum conditions (Fig. 43.24) is better than 4% across the characterized substrate area. Most film samples exhibit better than 95% transmission in the 0.5- to 25-μm wavelength range. Adjustment of the ion-source position for optimal sheet-resistance uniformity led to acceptable transmission uniformity since the latter was determined to be far less sensitive to the spatial distribution of average ion flux.

Equation (1) implies that the sheet resistance of ITO coatings should decrease proportionally with increasing film thickness. The measured sheet resistances of several coatings with different thicknesses are plotted in Fig. 43.29 along with the expected sheet resistance curve using the resistivity of

Fig. 43.26
Plot of sheet resistance of ITO coatings as a function of arriving oxygen-ion energy for a fixed ion flux and film thickness. Deposition with 500 eV oxygen-ion assist resulted in nonconducting film.
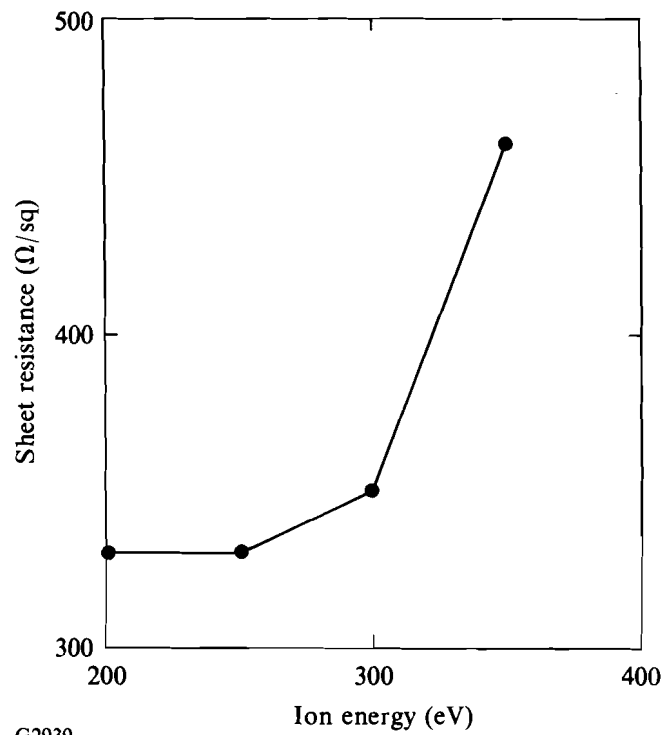
Fig. 43.27
Change in sheet resistance of ambient-temperature, IAD-processed ITO coatings obtained by varying ion-beam current at a fixed ion energy (200 eV) and film thickness (25 nm).

G2939

G2940

G2941
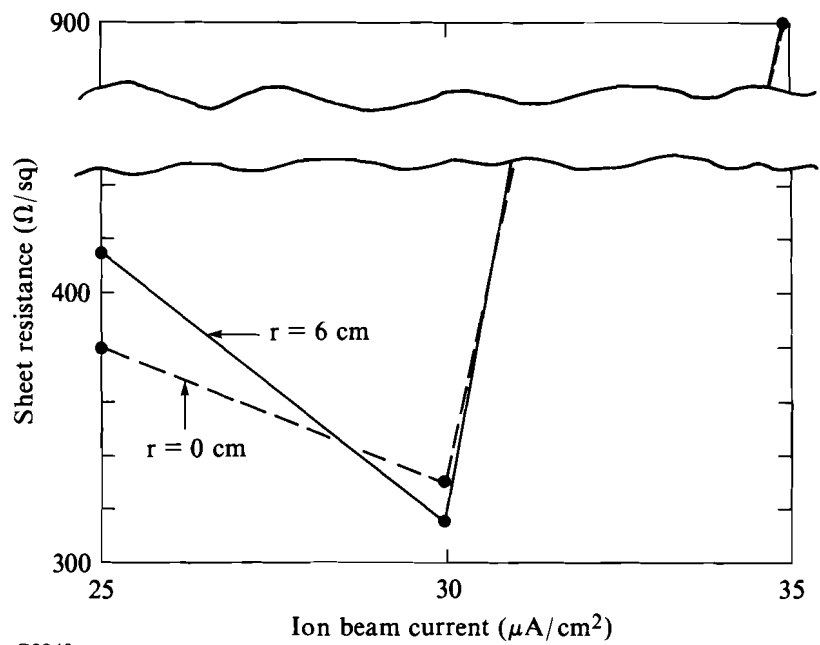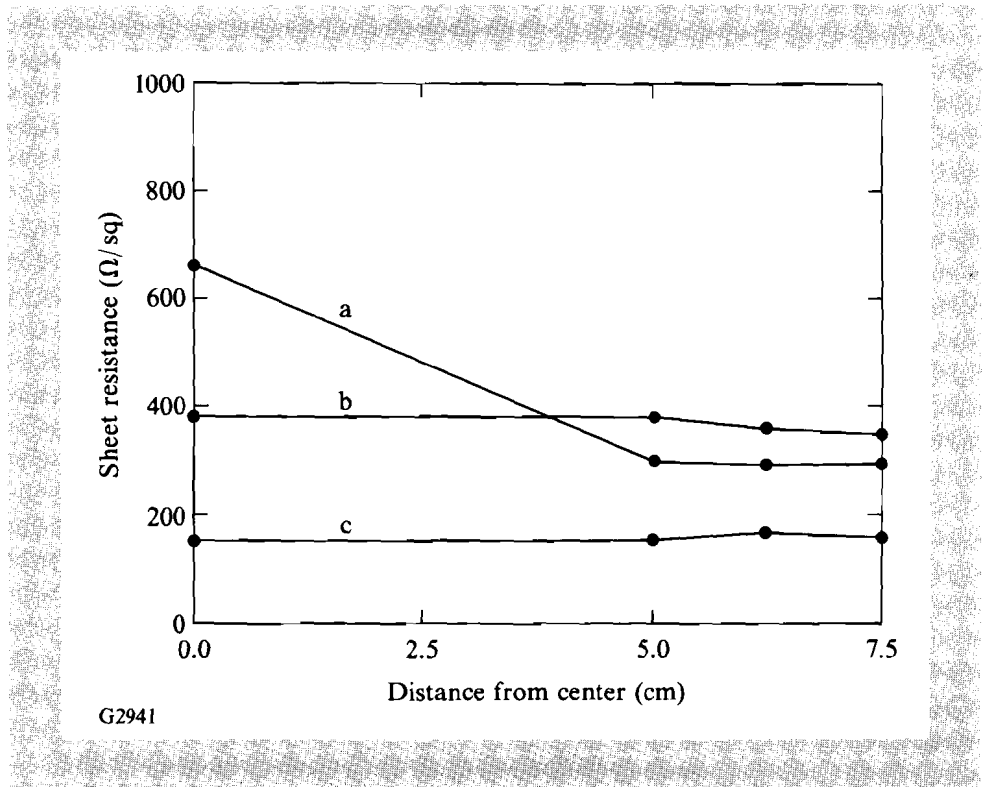
Fig. 43.28
Plot of sheet resistance as a function of radial distance from the center of substrate rotation: (a) before and (b), (c) after optimizing ion-source position. Curve (b) indicates uniformity of thin (25 nm) film, while curve (c) indicates uniformity of 250-nm-thick films.

G2942
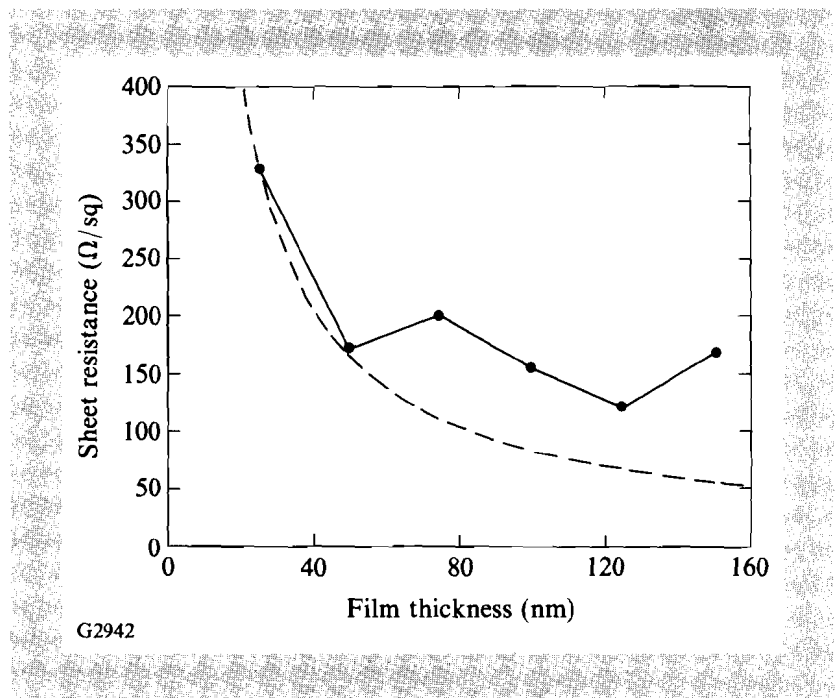
Fig. 43.29
Sheet resistance of ITO coatings deposited under optimized ambient-temperature IAD conditions as a function of film thickness. Dashed curve represents the expected values calculated from resistivity value obtained from 25-nm-thick film.

a 25-nm-thick film. The result indicates that the measured film resistances do not follow the expected thickness dependence. This could be caused by an increase in substrate temperature during the deposition. Thicker films (150 nm) saw a 54°C rise in chamber temperature in contrast to a 25°C rise for a thinner film (25 nm).

Following the initial measurements, several coating samples were baked in atmosphere at temperature gradations from 50°C to 125°C for several hours at each increment and recharacterized. This step was motivated by a conventional ITO deposition procedure that involves post-deposition annealing of films at temperatures above 300°C.[12] Subsequent measurements, summarized in Fig. 43.30, indicate that post-deposition baking induced a noticeable amount of improvement in both transparency and conductivity of the IAD-deposited ITO coatings. The increase in transparency, which is normally observed for heat-treated oxide films deposited in low ambient temperature, can be attributed to improved stoichiometry.[8] On the other hand, the increase in conductivity is most likely caused by the removal of excess oxygen, which can negate the tin-donor action by trapping carriers, and greater carrier mobility resulting from improved stoichiometry and crystallinity of the host indium oxide.[1,8,12]
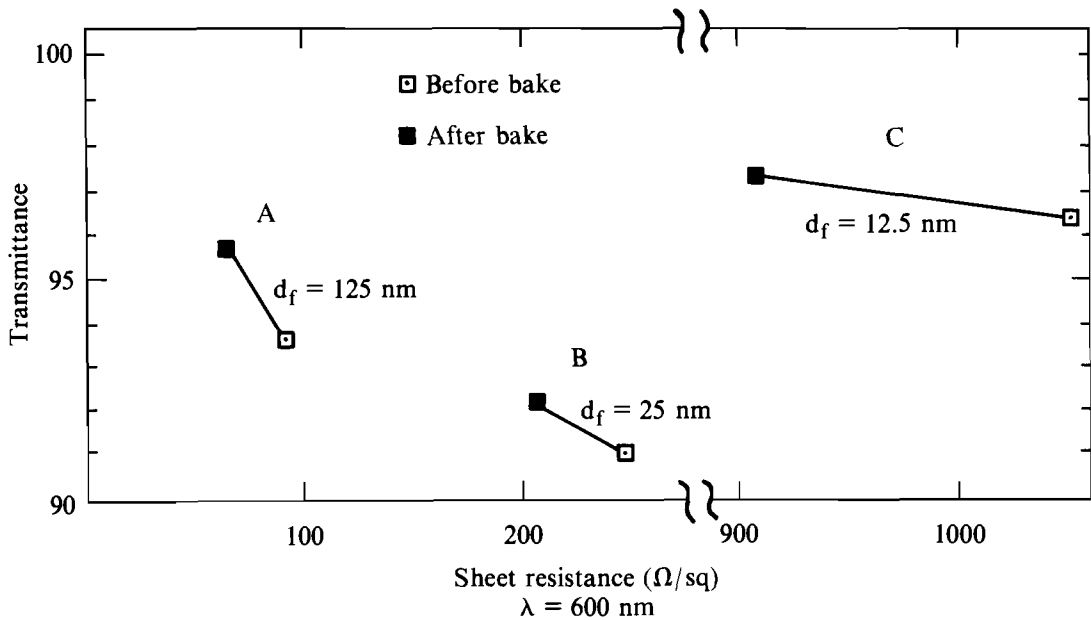
G2943

Fig. 43.30
Increase in transmission and conductivity of ITO coatings observed after 5 h of post-deposition bake at 125°C for films of different thicknesses (d_f) deposited under same IAD conditions.

Conclusion

The ambient-temperature, ion-assisted, electron-beam evaporation process is utilized to produce transparent conducting films of tin-doped indium oxide. Films as thin as 25 nm with better than 95% transmission in the 0.5- to 25-μm wavelength range with sheet resistance less than 350 Ω/sq were uniformly deposited onto a 15-cm-wide substrate area. The ambient temperature of the vacuum chamber did not rise above 54°C even during the deposition of 150-nm-thick films. For conventional reactive evaporation, such results are observed only when the films are deposited onto heated substrates ($T \geq 300$°C) or annealed at high temperature ($T \geq 400$°C) following the deposition.[1,9–12] Comparable values of transparency, sheet resistance, and uniformity are reported by only one other study[13] that was conducted with a cold-cathode ion source. This process was successfully used to coat small samples of KDP for testing as a longitudinal-mode Pockels cell.

REFERENCES

1. K. L. Chopra, S. Major, and D. K. Pandya, *Thin Solid Films* **102**, 1 (1983).

2. J. C. Lee, S. D. Jacobs, T. J. Kessler, and N. Van Lieu, "Profile Tunable Laser Beam Apodizer," presented at CLEO '89, Baltimore, MD, 24–28 April 1989.

3. D. J. Smith, C. J. Hayden, B. U. Krakauer, A. W. Schmid, and M. J. Guardalben, *Nat. Bur. Stand. (U.S.) Spec. Publ. 746*, Laser-Induced Damage in Optical Materials: 1985, 284 (July 1988).

4. M. S. Jin, M.S. thesis, University of Rochester, 1988.

5. "Electro-Optic Properties of KH_2PO_4 and Isomorphous," Cleveland Crystals, Inc., Cleveland, OH.

6. H. R. Kaufman, J. J. Cuomo, and J. M. E. Harper, *J. Vac. Sci. Technol.* **21**, 725 (1982).

7. L. I. Maissel and R. Glang, in *Handbook of Thin Film Technology* (McGraw-Hill, New York, 1970), Chap. 13, pp. 13-1–13-13.

8. J. L. Vossen, *Phys. Thin Films* **9**, 1 (1977).

9. P. J. Martin, R. P. Netterfield, and D. R. McKenzie, *Thin Solid Films* **137**, 207 (1986).

10. A. Hjortsberg, I. Hamberg, and C. G. Granqvist, *Thin Solid Films* **90**, 323 (1982).

11. M. Mizuhashi, *Thin Solid Films* **70**, 91 (1980).

12. A. Dietrich, K. Schmalzbauer, and H. Hoffmann, *Thin Solid Films* **122**, 19 (1984).

13. J. A. Dobrowolski *et al.*, *Appl. Opt.* **26**, 5204 (1987).

2.B   Transient-Surface Debye-Waller Effect

In the study of the interactions of ultrafast lasers with surfaces and the subsequent reactions, a key parameter is the time evolution of the surface temperature. Typically, this is determined for simple systems using a solution of the heat-diffusion equation. However, even in the simplest cases (e.g., the heating of a crystal surface that undergoes no phase change), such a solution may only provide the time evolution of the surface temperature with poor accuracy since many assumptions are built into these models. These assumptions include the temperature behaviors of the specific heat of the laser-irradiated material, its thermal conductivity, and laser-energy coupling. It has been previously demonstrated that second-harmonic generation at surfaces could be used as a surface structural probe[1] and, when resonantly enhanced, can also be used as a surface-temperature probe.[2] Surface temperatures deduced from the resonantly enhanced second-harmonic generation from an Ag(110) surface heated with nanosecond laser pulses have shown agreement with a heat-diffusion model.[2] However, this approach does not offer a general technique suitable to time-resolve the evolution of the surface temperature for different materials. Here we demonstrate the utilization of picosecond time-resolved reflection high-energy electron diffraction (RHEED) as a surface-lattice temperature probe.

Electron diffraction (both high energy and low energy) is a well-developed surface structural probe and has been utilized for many decades in surface studies.[3–7] The development of a picosecond-transmission electron-diffraction system was reported several years ago.[8] More recently we have demonstrated picosecond RHEED.[9] A detailed description of our ultrahigh vacuum picosecond RHEED system is given in Ref. 10.

Picosecond RHEED—A Surface-Temperature Probe

The basic idea of this technique is the utilization of a picosecond laser pulse to create an electron pulse with a comparable time duration. A schematic diagram of this technique is shown in Fig. 43.31. We use a Nd:YAG laser ($\lambda = 1.06$ μm) to irradiate the sample, while the electron probing pulse is generated by irradiation of a photocathode with the frequency-quadrupled Nd:YAG ($\lambda = 0.266$ μm). The photogenerated electrons are collimated and focused electrostatically making them suitable to obtain a good RHEED pattern from the studied crystal surface. Only a very small part of the Nd:YAG fundamental is converted to the ultraviolet; thus, most of the laser energy is available to irradiate the sample. By spatially delaying the fundamental from the ultraviolet laser pulse, it is possible to obtain RHEED patterns at times before, during, and after laser irradiation with up to a few-hundred-picoseconds time resolution.
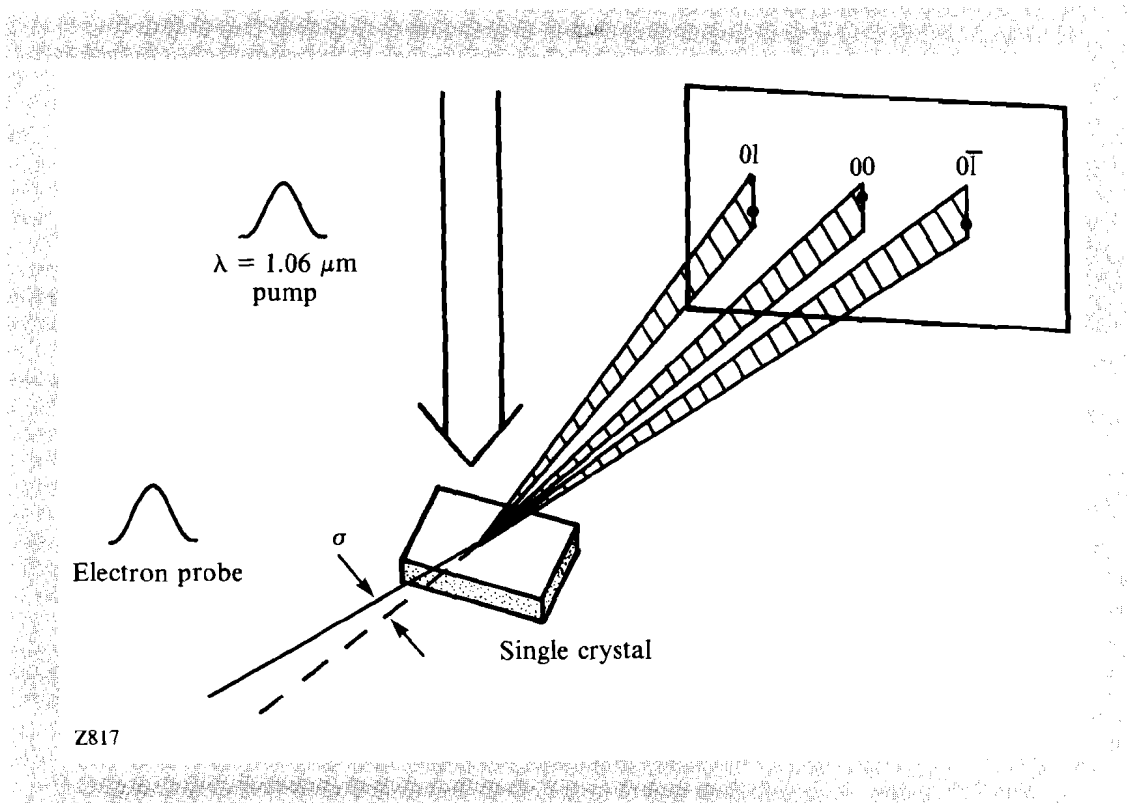
Fig. 43.31
Picosecond time-resolved reflection high-energy electron diffraction (RHEED).
The laser pump and electron probe are well synchronized.

The sensitivity of the diffraction pattern to temperature comes from the fact that as the temperature is raised, there is an increased atomic vibrational amplitude and, thus, an increased dephasing of the atomic scattering centers. This dephasing on the diffraction pattern reduces the number of electrons elastically scattered (i.e., to reduce the diffraction streak intensity). The reduced streak intensity shows up as an increased background that is

caused by the inelastically scattered electrons. Such a reduced intensity occurs with no widening of the diffraction streaks (or spots). This is known as the Debye-Waller effect, which was first analyzed by Debye for x-ray diffraction.[11]

Experimental Setup

The design of the photoactivated RHEED electron gun is similar to that of an x-ray streak camera. A 250-Å gold film deposited on a sapphire window is used as a photocathode. A single electrostatic lens is used to collimate and focus the electrons. A schematic diagram of the electron gun is shown in Fig. 43.32. For the current experiment, 14-keV electrons are used. The electrons are focused to a spot size of ~340 μm and have a pulse width comparable to the pulse width of the laser. Approximately 10^5 electrons are contained in each pulse.
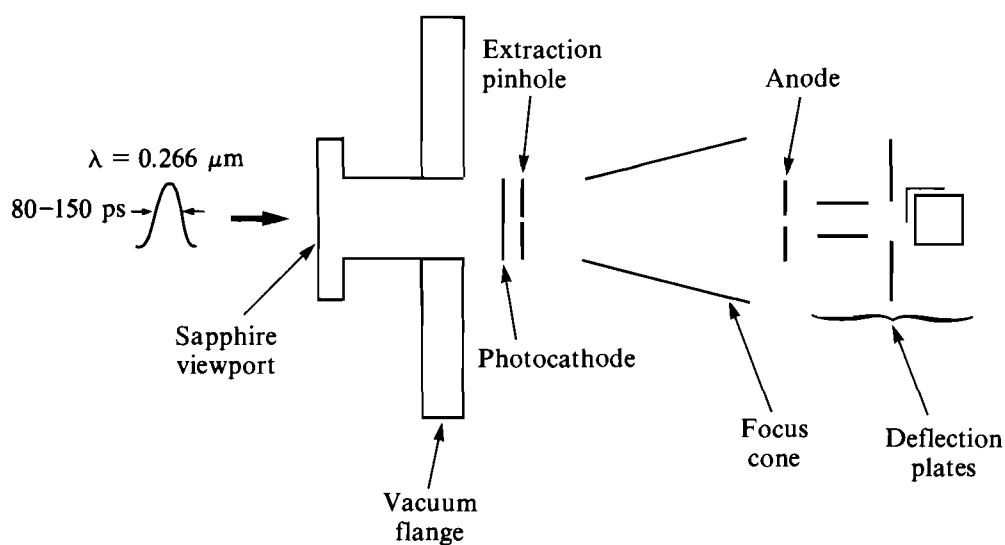
Fig. 43.32
A schematic of the photoactivated picosecond electron gun.

The picosecond RHEED system is assembled on a dedicated ultrahigh vacuum system (10^{-10} Torr). Conventional techniques of sample cleaning by argon-ion bombardment and annealing are performed prior to experiments.

A schematic diagram of the laser system used to drive the picosecond RHEED apparatus is shown in Fig. 43.33. A cw-pumped, mode-locked, Nd:YAG (λ = 1.06 μm) oscillator generates a 100-MHz train of about 120- to 300-ps FWHM pulses. A switchout consisting of a Pockels cell and two polarizers is used to select a pulse at a variable repetition rate up to
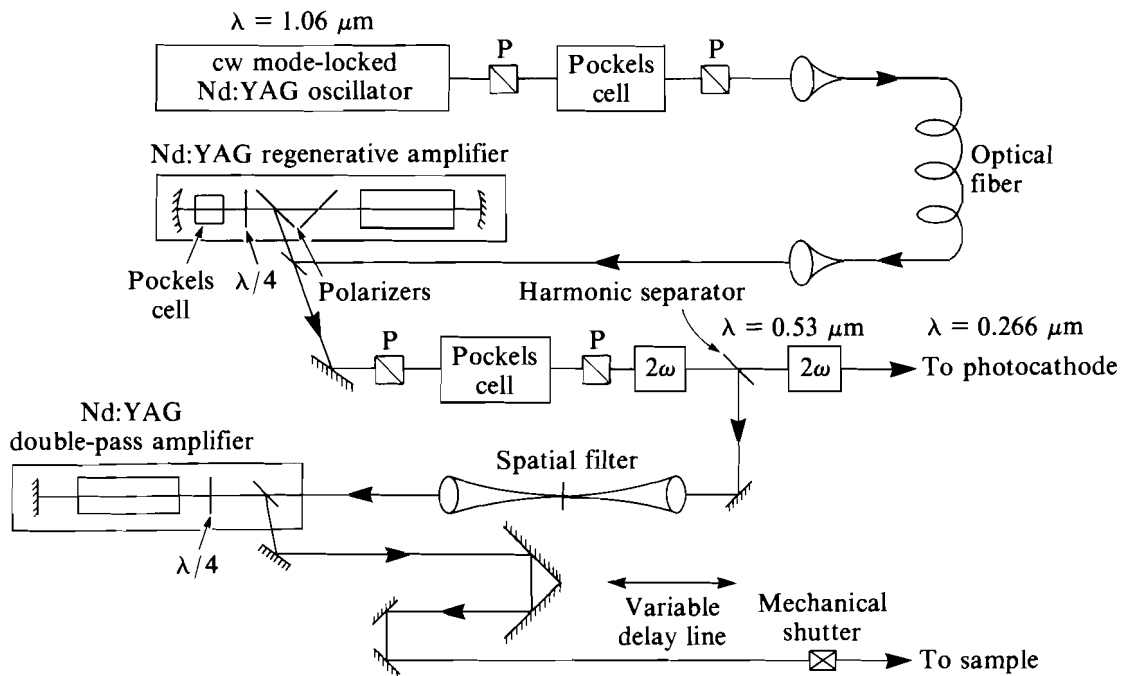
Fig. 43.33
A schematic diagram of the laser system driving the picosecond RHEED apparatus.

1.5 kHz. The selected oscillator pulse is coupled to the cw-pumped regenerative amplifier.[12] Pulse injection is accomplished by applying a fast step to the Pockels cell in the regenerative amplifier cavity.[13] The magnitude of this voltage step is to achieve quarter-wave retardation. This causes a cavity round trip of full-wave retardation, thus minimizing cavity losses and trapping the injected pulse. After ~40 round trips, the pulse inside the regenerative-amplifier cavity builds up to its peak value and is cavity dumped by applying a second voltage-step function causing the Pockels cell to have half-wave retardation.[13]

The laser pulse width from the regenerative amplifier is nearly equal to that of the oscillator; that is, pulse broadening in the regenerative amplifier is negligible. The pulse width can vary from day to day, depending on the alignment of the mode-locker and setting of the cavity length.

The energy content of the principal pulse is typically ~0.4 mJ. To increase the ratio of the energy content of the principal pulse to that of other pulses, an external switchout consisting of a Pockels cell and two polarizers is used. After the external switchout, the ratio is observed to be better than several hundred to one.

The output of the external Pockels cell is frequency doubled. Less than 1% conversion efficiency is needed. The fundamental and the frequency-doubled Nd:YAG pulses are split in a harmonic separator. The green ($\lambda = 0.53~\mu$m) pulses are further doubled to generate ultraviolet pulses ($\lambda = 0.266~\mu$m). These ultraviolet photons are utilized to pump the photocathode.

The fundamental pulse is spatially filtered and passes through a 7-mm double-pass amplifier. During system alignment, the double-pass amplifier is not activated; for heating experiments, the double-pass amplifier is activated. This is typically operated up to 30 mJ at an 8-Hz repetition rate. An optical delay line is used to vary the timing between the fundamental pulse and the ultraviolet pulse that drives the photocathode of the electron gun.

For electron detection, we use gated microchannel plates (MCP's) proximity focused to a P-47 phosphor screen. Since laser heating below the threshold of surface damage is reversible, we can average over many shots to enhance our signal. The maximum repetition rate of this system when no MCP's are used is limited only by the laser repetition rate, since the decay time of the P-47 phosphor screen is ~0.15 μs. When MCP's are used, the maximum repetition rate is limited by their dead time that typically limits the system to a few kilohertz.[14]

To obtain quantitative information on surface structure and temperature from the picosecond RHEED patterns, it is necessary to determine the scattering angles and the diffraction intensity. For the current experiments we use a linear array detector, an optical multichannel analyzer (OMA), to observe a line across the diffraction pattern. A RHEED pattern of the Pb(110) surface obtained by using picosecond electron pulses is shown in Fig. 43.34. The approximate location of the line scan across the image observed by the OMA is indicated.

Measurements of Transient Debye-Waller Effect

We have performed measurements of the surface Debye-Waller effect with a few-hundred-picosecond time resolution on a Pb(110) crystal. By measuring the distance from the undiffracted electron beam to the pattern's shadow edge and knowing the distance of the phosphor screen assembly to the sample, we estimate the electron beam's angle of incidence on the sample to be ~3°. The $\lambda = 1.06~\mu$m fundamental is used to heat the surface of the crystal (at near normal incidence), while the electron pulses are used to probe the surface in the manner previously described. The system is operated at 8-Hz repetition rate and provides a maximum energy of ~20 mJ per pulse to the surface of the sample. The infrared heating pulse passes through an optical delay line before hitting the sample. The timing of the heating laser pulse and the electron pulse at the sample is set by adjustments of the delay line.
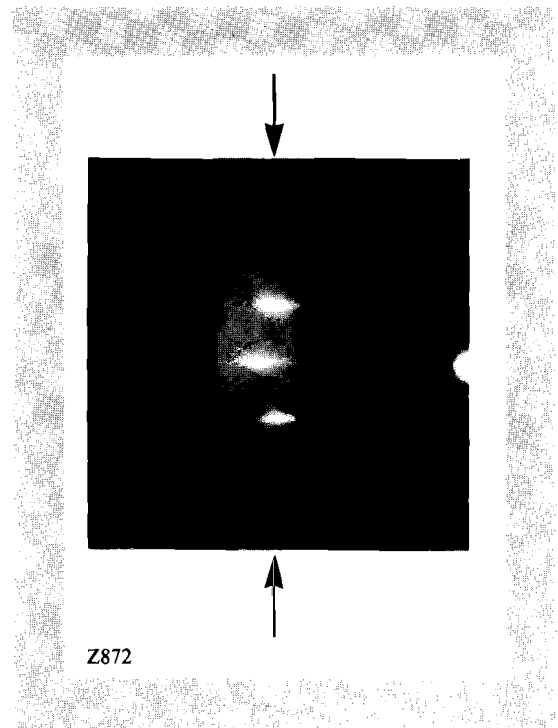
Fig. 43.34
A RHEED pattern of Pb(110) taken using many picosecond electron pulses. The arrows indicate the approximate location of the line scan obtained by lens imaging this pattern onto an optical multichannel analyzer (OMA).

To enhance our signal, we insert a mechanical shutter in the IR beam path that allows every other laser-heating pulse to interact with the sample. Two line scans are obtained for determined experimental conditions: the first is with no laser heating; the second is with laser heating. Each scan is stored in a separate memory. This process is repeated at various positions of the delay line. Scans with and without laser heating are sorted and averaged in separate memories. This averaging effectively compensates for shot-to-shot fluctuations and for long-term drifts in the UV laser intensity and electron gun. However, pulse-to-pulse fluctuations and long-term drifts in the heating IR pulse cannot be compensated for using this method. A histogram of the laser-heating pulse energy indicates that, for about 90% of the pulses, the pulse energy falls within ±10% of the average. Long-term stability of the heating laser is regularly monitored during the experiment.

For a representative experiment, line scans through the diffraction pattern obtained at various times relative to the arrival of the laser-heating pulse to the sample are shown in Fig. 43.35. The relative peak heights are determined by the crystal alignment and the positioning of the linear array detector. The upper scans correspond to no laser heating while the lower scans correspond to the laser-heated surface. The OMA is set to average 480 shots per scan. From this figure, we can see that there is a significant change in the intensity of the diffraction rods as the laser-heating pulse strikes the sample. This change decreases as the surface of the sample cools mainly by heat diffusion to the bulk.

The time-resolved results are related to the lattice temperature by performing a static heating experiment. We heat the sample on a resistively
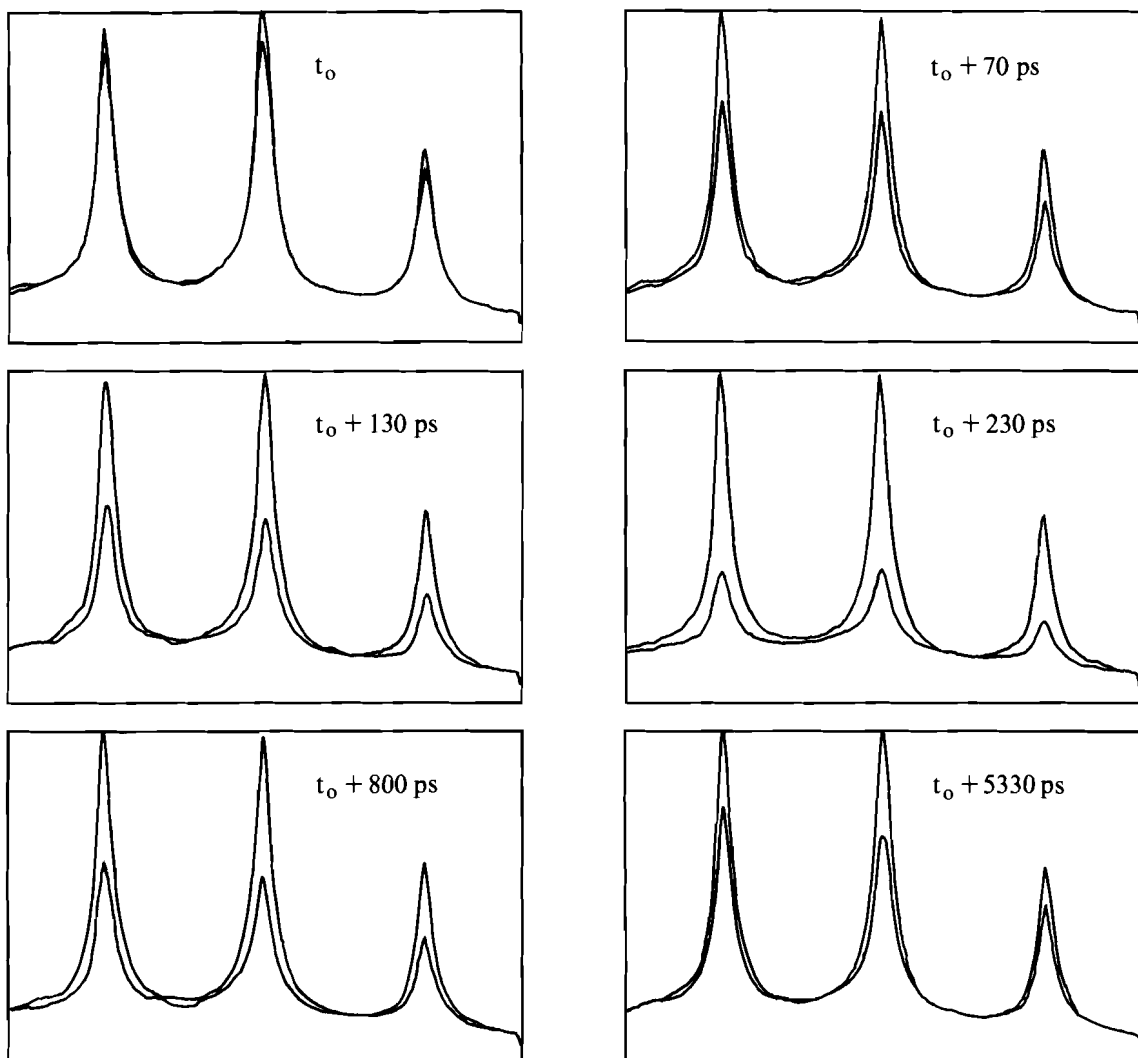
Z873

Fig. 43.35
Line scans through the diffraction patterns at various times. The upper scans correspond to an unheated surface while the lower scans correspond to a laser-heated surface.

heated stage and observe the intensity of the diffraction pattern as a function of the sample temperature, measured by thermocouples located on the surface of the stage just above and below the sample. In this way, we determine the normalized RHEED streak intensity when the sample is heated from room temperature to a given temperature. Results of such a measurement of the average change in one of the streaks (left peak in Fig. 43.35) are shown in Fig. 43.36, along with an exponential fit of the temperature versus RHEED streak intensity normalized to the room-temperature streak intensity. By comparing these intensity measurements
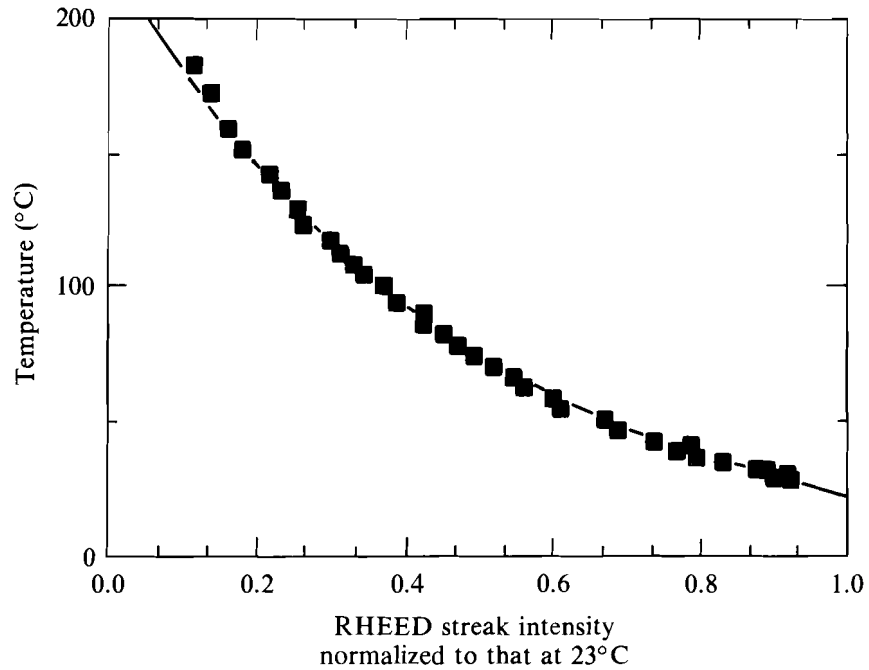
Z883

Fig. 43.36
Temperature versus normalized RHEED streak intensity. The Pb(110) sample is
heated on a hot stage. The temperature is measured using thermocouples. The
location of the line scan across the diffraction pattern is the same as that for pulsed
laser heating. An exponential fit is made to the data and is used to obtain the time-
resolved surface temperature in Fig. 43.37.

under different temperatures with measurements taken for picosecond laser
heating, we obtain the time-resolved surface temperature with up to a few-
hundred-picosecond time resolution. The validity of the temperature
calibration, which is based on a comparison of the magnitude of the surface
Debye-Waller effect measured under static conditions with that measured
under dynamic heating conditions, was not directly tested. However, this
calibration should hold if (1) the time scale of our measurements is longer
than that needed for equilibrium to be established between the electrons and
the lattice in our sample (in metals, at room temperature or higher, this
typically occurs within a few picoseconds[15]); (2) no surface phase
transformation occurs; and (3) no accumulated surface modifications occur
by repeated laser heating. These conditions appear to be fulfilled in the
experiments reported here.

Based on this calibration, we obtain the time evolution of the surface-
temperature rise caused by laser heating. Results from an experimental run
are shown in Fig. 43.37, along with the decay of the surface-temperature
rise obtained from a heat-diffusion model.
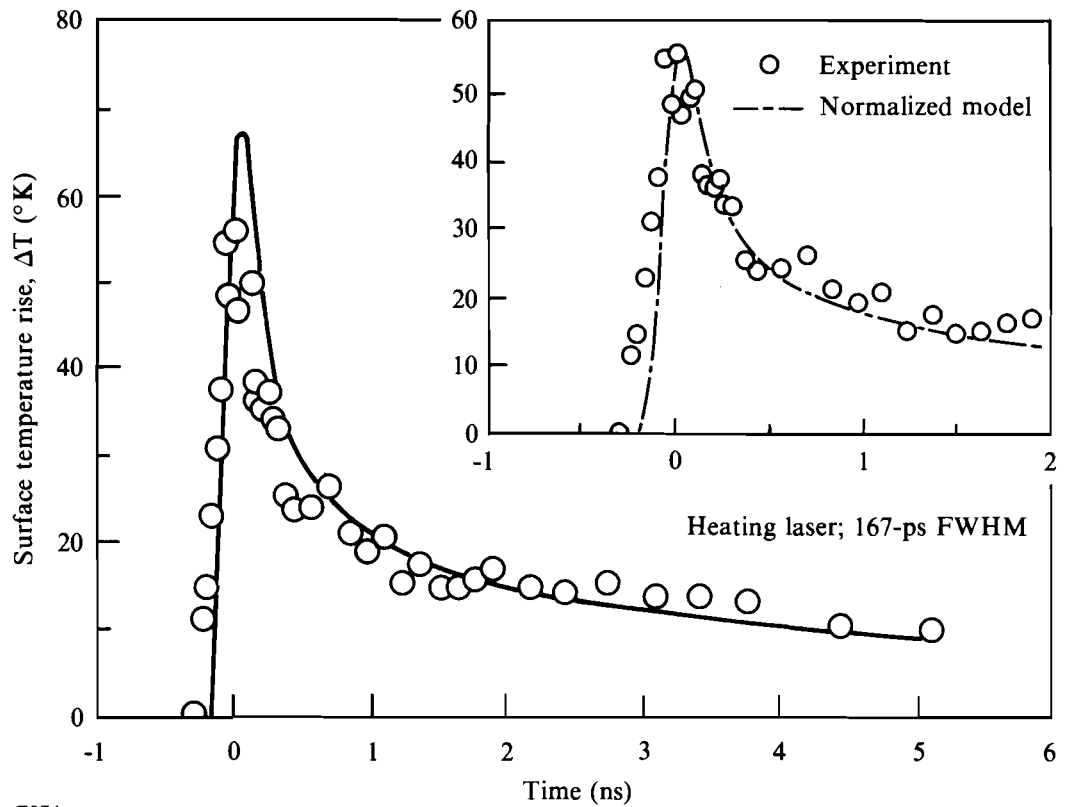
Fig. 43.37
Transient surface temperature rise of Pb(110) irradiated with 3.5×10^7 W/cm^2 peak intensity, 167-ps FWHM, Nd:YAG ($\lambda = 1.06 \mu$m) laser pulses. Experimental results are obtained from the transient surface Debye-Waller effect on RHEED intensity using the calibration obtained in Fig. 43.36. The solid line is obtained from a numerical heat diffusion model. In the inset, the peak temperature from the model is normalized to that from the experiment.

Heat-Diffusion Model

A numerical solution of the surface temperature is obtained from a one-dimensional heat-diffusion model based on the equation[16]

$$C[dT(z,t)/dt] = K[d^2T(z,t)/dz^2] + I(1-R)\alpha e^{-\alpha z}f(t),$$

where C is the heat capacity per unit volume, $T(z,t)$ is the temperature profile at distance z normal to the sample surface ($z = 0$), t is time, K is the thermal conductivity, I is the laser peak intensity, α is the absorption per unit length, and $f(t)$ is the time dependence of the laser pulse that is assumed Gaussian. The values of parameters in this equation are listed in Table 43.II.

Table 43.II: Values of physical constants used for the calculation shown in Fig. 43.37.

C: Heat capacity per unit volume (J/m^3 K)[a]	1.47×10^6
K: Thermal conductivity (W/m K)[a]	34.6
I: Laser peak intensity (W/cm^2)	3.5×10^7
R: Reflectivity [b]	0.857
α: Absorption coefficient(m^{-1})[b]	6.77×10^7

[a] *Amercian Institute of Physics Handbook*, 3rd ed. (McGraw-Hill, New York, 1972).
[b] From $R = [(n-1)^2 + k^2]/[(n+1)^2 + k^2]$ and $\alpha = 4\pi k/\lambda$, where n and k are the real and imaginary parts of the complex index of refraction. [A. I. Golovashkin and G. P. Motulevich, *Sov. Phys. JETP* **26**, 881 (1968)].

Z895

As shown in Fig. 43.37, the surface-temperature rise obtained using the transient-surface Debye-Waller effect on the picosecond RHEED pattern shows general agreement with that predicted by a heat-diffusion model. However, an uncertainty in the model is the value of the reflectivity and absorptivity. For these values we have relied on the measurements of Golovashkin and Motulevich rather than measuring it for our sample. Nonlocal effects on the thermal conductivity, which can arise if the temperature gradient is significant within a mean-free path of the heat carriers,[17] i.e., hot electrons, are also not included in the model. Such nonlocal effects were shown to reduce heat conductivity.[17]

Conclusion

We have demonstrated the use of picosecond RHEED as a time-resolved surface-temperature probe. The temperature measurement is based on the surface Debye-Waller effect that results in a reduction of the number of elastically scattered electrons with lattice heating, thus reducing the RHEED streak intensity. Our time-resolved measurements of the picosecond-laser-heated Pb(110) surface show general agreement with a heat-diffusion model.

The time resolution, in the current experiments, is limited to a few hundred picoseconds. However, the extension of time-resolved RHEED techniques, as a temperature probe of recurrent events (e.g., simple surface heating), to a subpicosecond resolution should be possible. The technology required to accomplish this is similar to that currently utilized in subpicosecond streak cameras.[18] The temperature-measurement accuracy depends on the overall stability of the system and its repetition rate. For the data shown in Fig. 43.37 we estimate an accuracy of ±15 K. However, much higher accuracy can be

achieved by increasing the repetition rate and collecting data for a specific narrow window of laser-pulse energy.

The technique of picosecond RHEED offers both surface selectivity and temperature sensitivity. In addition to its utilization as a time-resolved structural and temperature probe of fast-surface processes, it can also be used to study the thermal properties of extremely thin films (up to a few monolayers).

ACKNOWLEDGMENT

REFERENCES

1. C. V. Shank, R. Yen, and C. Hirlimann, *Phys. Rev. Lett.* **51**, 900 (1983).

2. J. M. Hicks, L. E. Urbach, E. W. Plummer, and H.-L. Dai, *Phys. Rev. Lett.* **61**, 2588 (1988).

3. E. Bauer, *Techniques of Metal Research*, Vol. II, Part 2, edited by R. F. Bunshah (Interscience, New York, 1969), p. 501.

4. P. J. Estrup and E. G. McRae, *Surf. Sci.* **25**, 1 (1971).

5. C. B. Duke and R. L. Park, *Phys. Today* **25**, 23 (1972).

6. D. Lichtman, *Methods of Surface Analysis*, Vol. I, edited by A. W. Czanderna (Elsevier Sci. Pub., New York, 1975), p. 39.

7. A. U. MacRae, *Science* **139**, 379 (1963).

8. G. Mourou and S. Williamson, *Appl. Phys. Lett.* **41**, 44 (1982).

9. H. E. Elsayed-Ali and G. A. Mourou, *Appl. Phys. Lett.* **52**, 103 (1988).

10. H. E. Elsayed-Ali and J. W. Herman, *Rev. Sci. Instrum.* **61**, 1636 (1990).

11. C. Kittel, *Introduction to Solid State Physics*, 5th edition (Wiley, New York, 1976), p. 63.

12. I. N. Duling III, T. Norris, T. Sizer II, P. Bado, and G. A. Mourou, *J. Opt. Soc. Am. B* **2**, 616 (1985).

13. P. Bado and M. Bouvier, *Rev. Sci. Instrum.* **56**, 1744 (1985).

14. J. L. Wiza, *Nucl. Instrum. Methods* **162**, 587 (1979).

15. H. E. Elsayed-Ali, T. B. Norris, M. A. Pessot, and G. A. Mourou, *Phys. Rev. Lett.* **58**, 1212 (1987).

16. J. H. Bechtel, *J. Appl. Phys.* **46**, 1585 (1975).

17. F. Claro and G. D. Mahan, *J. Appl. Phys.* **66**, 4213 (1989).

18. K. Kinoshita, M. Ito, and Y. Suzuki, *Rev. Sci Instrum.* **58**, 932 (1987).

Section 3

NATIONAL LASER USERS FACILITY NEWS

During the third quarter of FY90 NLUF activities centered on (1) experiments by **H. Griem** (University of Maryland) and **C. Hooper** (University of Florida) performed on the OMEGA laser; (2) an Air Force-funded experiment by **G. Banas** (University of Illinois) on the GDL laser; and (3) an NLUF Steering Committee meeting. In addition, **A. Honig** (Syracuse University) ran a fit check of his cold-entry, target-handling system using the OMEGA target chamber.

J. Marino of H. Griem's group used a series of target shots on the OMEGA laser to measure the characteristics of XUV emission from multilayer targets. The time dependence of the x-ray spectral emission was measured with the SPEAXS instrument; the XUV spectral time dependence was measured with the University of Maryland's McPigs spectrograph. The data collected from these target shots has been taken to Maryland for analysis.

C. Hooper and several students are collaborating with LLE scientists to measure high-density implosions of argon-filled plastic shells. The first series of shots used 250-μm-diam targets filled with 2, 5, and 10 atm of argon. The time dependence of the Ar emission was measured with the SPEAXS diagnostic. In addition, several other x-ray instruments were used to characterize the x-ray emission of these targets. The data is being

digitized at LLE while the analysis is proceeding at both LLE and the University of Florida.

A. Honig has been constructing a cold-entry, target-handling system for the OMEGA target chamber. This system is necessary for the implosion of spin-polarized targets for the Syracuse NLUF experiment and will be useful for future gas-filled, plastic-microballoon targets needed for ICF. The fit check to the OMEGA target chamber identified areas of work for the system to mate to the OMEGA cryogenic shroud. This work is proceeding at Syracuse and additional checks are planned for the target chamber.

G. Banas is collaborating with **H. Elsayed-Ali** of LLE to measure the effect of laser-shock hardening of metal weldments. This work was approved for laser time but not DOE funding for FY90. Since the Steering Committee meeting, these investigators have received funding from the Air Force and are proceeding with experiments on the GDL laser. The GDL laser is used at a 1.054-μm wavelength and directly illuminates a weldment. The weldment is then characterized at the University of Illinois.

The NLUF Steering Committee met 24 April 1990 to review proposals for FY91. There were 11 proposals submitted for consideration. Six of these proposals were recommended for laser time and funding by DOE. The approved experiments for FY91 were

(1) Time-Resolved Emission and Absorption Spectroscopy of High-Density Plasmas in Spherical and Planar Geometry;

(2) Study of the Sodium-Neon Photopumped X-Ray Laser Using High-Power Laser Irradiation of High-Density Planar Gas Jet to Create the Neon Lasand;

(3) Fusion with Highly Spin Polarized HD and D_2;

(4) Experimental Studies of Radiative Properties of High Energy Density Matter;

(5) Atomic Structure of Ni-Like, Soft X-Ray Lasing Ions;

(6) Development of a New Plasma Diagnostic of the Critical Surface and Studies of the Ion Acoustic Decay Instability Using Collective Thomson Scattering.

ACKNOWLEDGMENT

Section 4
LASER SYSTEM REPORT

4.A   GDL Facility Report

During the third quarter of FY90 the GDL oscillator was successfully converted to a 50-MHz drive for synchronization and timing. GDL operations concentrated on the four main experimental programs: x-ray laser, shine-through, Thomson scattering, and OMEGA Upgrade support. Additional developmental research was performed on a regenerative amplifier for the pulse-shaping experiments, apodizer testing, and film studies. G. Banas from University of Illinois performed the only NLUF experiment this quarter.

A summary of GDL operation this quarter follows:

Beamline Test, Calibration, Tuning, and		
Laser Alignment Shots		211
Apodizer Tests		2
Film Studies		32
Target Shots		
Shine-through		45
X-ray Laser		36
NLUF User		47
Thomson Scattering		20
	TOTAL	393

4.B   OMEGA Facility Report

The OMEGA laser system remained fully operational for the third quarter of FY90. Several minor laser modifications were incorporated and three primary experimental programs supported.

A redesigned microwave modulator utilizing a waveguide-coupled cavity has resulted in the capability to create up to 5 Å of laser bandwidth. This new modulator and tunable waveguide provided more reliable broadband phase-converted irradiation conditions for experimentation.

Many target shots were taken to assess the variation of performance as a function of laser bandwidth. One experiment used a single beam of OMEGA to explore the Stimulated Rotational Raman Scattering (SRRS) threshold dependence on bandwidth and dispersion. The first round of SRRS data collection was finished early in the quarter and results will be reported in an upcoming LLE Review. Secondly, implosions were investigated in ongoing yield/density programs. These studies included sequences of LLE-fabricated plastic targets, Argon targets (in collaboration with NLUF users from the University of Florida), and surrogate cryogenic targets of deuterated CH. The last campaign run on OMEGA this quarter involved irradiation of flat targets with eight beams per side. The beams were staggered in time to create a large-scale plasma for various laser-plasma interaction instability investigations. These experiments gave interaction data with unique laser conditions designed specifically to create instability signatures.

A shot summary on OMEGA for this quarter follows:

Driver Line		35
Laser Test		52
Target		125
Software		12
	TOTAL	224

PUBLICATIONS AND CONFERENCE PRESENTATIONS

Publications

S. Augst, D. D. Meyerhofer, C. I. Moore, and J. Peatross, "Tunneling Ionization and Harmonic Generation in Krypton Gas Using a High-Intensity, 1-μm, 1-ps Laser," *Femtosecond to Nanosecond High-Intensity Lasers and Applications* (SPIE, Bellingham, WA, 1990), Vol. 1229, pp. 152–158.

G. Banas, F. V. Lawrence, Jr., J. M. Rigsbee, and H. E. Elsayed-Ali, "Laser Shock Hardening of Welded Maraging Steel," in *Surface Engineering: Current Trends and Future Prospects*, edited by S. A. Meguid (Elsevier Applied Science, London and New York, 1990), pp. 280–290.

H. Chen, Y.-H. Chuang, R. Epstein, D. D. Meyerhofer, S. Uchida, and B. Yaakobi, "Spectroscopic Investigation of Plasma Produced with High-Intensity, 1-μm, 1-ps Laser Pulses," *Femtosecond to Nanosecond High-Intensity Lasers and Applications* (SPIE, Bellingham, WA, 1990), Vol. 1229, pp. 182–189.

P. C. Cheng, S. P. Newberry, H. Kim, M. D. Wittman, and S. Hwang, "X-Ray Microradiography and Shadow Projection X-Ray Microscopy," in *Modern Microscopy*, edited by P. J. Duke and A. G. Michette (Plenum Publishing Corporation, New York, 1990), pp. 87–118.

J. Delettrez, D. K. Bradley, P. A. Jaanimagi, and C. P. Verdon, "Effect of Barrier Layers in Burnthrough Experiments with 351-nm Laser Illumination," *Phys. Rev. A* **41**, 5583–5593 (1990).

H. E. Elsayed-Ali, "Comment on 'Thermal Response of Metals to Ultrashort-Pulse Laser Excitation'," *Phys. Rev. Lett.* **64,** 1846 (1990).

H. E. Elsayed-Ali and J. W. Herman, "Transient Surface Debye-Waller Effect" (invited paper), *Picosecond and Femtosecond Spectroscopy from Laboratory to Real World* (SPIE, Bellingham, WA, 1990), Vol. 1209, pp. 76–85.

H. E. Elsayed-Ali and J. W. Herman, "Ultrahigh Vacuum Picosecond Laser-Driven Electron Diffraction System," *Rev. Sci. Instrum.* **61,** 1636–1647 (1990).

C. J. McKinstrie and G. G. Luther, "The Modulational Instability of Colinear Waves," *Phys. Scr.* **30,** 31–40 (1990).

D. D. Meyerhofer, H. Chen, Y.-H. Chuang, J. Delettrez, R. Epstein, S. Uchida, and B. Yaakobi, "High Intensity, Short-Pulse (1-ps), Laser-Plasma Interaction at 1 μm," *Femtosecond to Nanosecond High-Intensity Lasers and Applications* (SPIE, Bellingham, WA, 1990), Vol. 1229, pp. 119–127.

T. B. Norris, X. J. Song, G. Wicks, W. J. Schaff, L. F. Eastman, and G. A. Mourou, "Electric Field Dependence of the Tunneling Escape Time of Electrons from a Quantum Well," in *OSA Proceedings on Picosecond Electronics and Optoelectronics,* edited by T. C. L. G. Sollner and D. M. Bloom (OSA, Washington, DC, 1989), Vol. 4, pp. 121–123.

T. B. Norris, N. Vodjdani, B. Vinter, C. Weisbuch, and G. A. Mourou, "Time-Resolved Observation of Luminescence from a Charge-Transfer State in Double Quantum Wells," in *OSA Proceedings on Picosecond Electronics and Optoelectronics,* edited by T. C. L. G. Sollner and D. M. Bloom (OSA, Washington, DC, 1989), Vol. 4, pp. 106–109.

M. Pessot, J. Squier, G. Mourou, and D. J. Harter, "Amplification of 100 fs mJ Pulses in Alexandrite Using Chirped Pulse Techniques," in *OSA Proceedings on Tunable Solid State Lasers,* edited by M. L. Shand and H. P. Jenssen (OSA, Washington, DC, 1989), Vol. 5, pp. 44–49.

Forthcoming Publications

S. H. Batha, D. D. Meyerhofer, A. Simon, and R. P. Drake, "Enhanced Scattering from Laser-Plasma Interactions," to be published in *Physical Review.*

T. Boehly, R. S. Craxton, R. Epstein, M. Russotto, and B. Yaakobi, "X-Ray Lasing in Thick Foil Irradiation Geometry," to be published in *Optics Communications.*

S. H. Chen and M. L. Tsai, "New Thermotropic Chiral Nematic Copolymers Using (1S, 2S, 3S, 5R)-(+)- and (1R, 2R, 3R, 5S)-(-)-Isopinocampheol as Building Blocks," to be published in *Macromolecules.*

H. C. Chen, G. Mourou, and R. Knox, "Time-Resolved Electron Diffraction from Pulse-Excited Crystalline Gold Films," to be published in the *Proceedings of 1989 Materials Research Society Fall Meeting: Beam-Solid Interactions*, Boston, MA, 27 November–2 December 1989; and in *Physical Review Letters*.

P. C. Cheng, V. H-K. Chen, H. Kim, and R. E. Pearson, "A Real-Time EPI-Fluorescent Confocal Microscope," to be published in *Journal of Microscopy*.

P. C. Cheng, V. H-K. Chen, H. Kim, and R. E. Pearson, "An EPI-Fluorescent Spinning-Disk Confocal Microscope," to be published in the *Proceedings of the 47th Annual Meeting of Electron Microscopy Society of America (EMSA)*, Austin, TX, 14–18 August 1989.

H. E. Elsayed-Ali and J. W. Herman, "Picosecond Transient Surface Temperature Measurement by Reflection High-Energy Electron Diffraction," to be published in the *Proceedings of the Topical Meeting on Ultrafast Phenomena*, Monterey, CA, 14–17 May 1990.

H. E. Elsayed-Ali and J. W. Herman, "Picosecond Time-Resolved Surface-Lattice Temperature Probe," to be published in *Applied Physics Letters*.

H. E. Elsayed-Ali, T. Juhasz, G. O. Smith, and W. E. Bron, "Femtosecond Thermoreflectivity and Thermotransmissivity of Polycrystalline and Single-Crystalline Gold Films," to be published in *Physical Review Letters*.

H. E. Elsayed-Ali, T. Juhasz, G. O. Smith, and W. E. Bron, "Femtosecond Thermomodulation of Single-Crystalline and Polycrystalline Gold Films," to be published in the *Proceedings of the Topical Meeting on Ultrafast Phenomena*, Monterey, CA, 14–17 May 1990.

E. M. Epperlein, "Electron Kinetics in Laser-Driven Inertial Confinement Fusion," to be published in the *Proceedings of the Topical Conference on Research Trends in Nonlinear and Relativistic Effects in Plasmas*, La Jolla, CA, 5–8 February 1990.

E. M. Epperlein, "A Kinetic Theory of Laser Filamentation in Plasmas," to be published in *Physical Review Letters*.

R. Epstein and S. Skupsky, "Anticipated Improvement in Laser Beam Uniformity Using Distributed Phase Plates with Quasi-Random Patterns," to be published in *Journal of Applied Physics*.

R. Q. Gram, M. D. Wittman, C. Immesoete, H. Kim, R. S. Craxton, N. Sampat, S. Swales, G. Pien, J. M. Soures, and H. Kong, "Uniform Liquid-Fuel Layer Produced in a Cryogenic Inertial Fusion Target by a Time-Dependent Thermal Gradient," to be published in *Journal of Vacuum Science and Technology A*.

C. Immesoete, S. Scarantino, H. Kim, and L. Forsley, "Computer-Assisted Microballoon Selection for Inertial Confinement Fusion Targets," to be published in *Journal of Vacuum Science and Technology A*.

S. D. Jacobs, "Optical Materials: Improved Building Blocks for Better Lasers," to be published in *Chemtech*.

H. Kim, C. K. Immesoete, and S. Scarantino, "Computer-Assisted Microballoon Selection for Inertial Fusion Targets," to be published in the *Proceedings of the Seventh Target Fabrication Specialists Meeting*, Livermore, CA, 25–29 September 1989.

H. Kim, R. Q. Gram, M. D. Wittman, C. Immesoete, R. S. Craxton, N. Sampat, S. Swales, G. Pien, and J. M. Soures, "Uniform Liquid Fuel Layer Produced in a Cryogenic Target by a Time-Dependent Thermal Gradient," to be published in the *Proceedings of the Seventh Target Fabrication Specialists Meeting*, Livermore, CA, 25–29 September 1989.

L. E. Kingsley and W. R. Donaldson, "Electro-Optic Imaging of Surface Electric Fields in High-Power Photoconductive Switches," to be published in *IEEE Transactions on Electron Devices*.

J. C. Lambropoulos and S.-S. Hwang, "Film Thermal Conductivity and Laser Damage Resistance of Optical Thin Films," to be published in the *Proceedings of a Symposium on Electro-Optics and Non-Linear Optics*, 1st International Congress on Ceramic Science and Technology, Anaheim, CA, 1–3 November 1989.

J. C. Lee, S. D. Jacobs, and K. J. Skerrett, "Laser Beam Apodizer Utilizing Gradient-Index Optical Effects in Liquid Crystals," to be published in *Optical Engineering*.

J. C. Lee, S. D. Jacobs, T. Gunderman, A. Schmid, T. J. Kessler, and M. D. Skeldon, "TEM_{00} Mode and Single Longitudinal Mode Laser Operation with a Cholesteric Liquid Crystal Laser End Mirror," to be published in *Optics Letters*.

G. G. Luther, C. J. McKinstrie, and A. L. Gaeta, "The Transverse Modulational Instability of Counterpropagating Light Waves," to be published in the *Proceedings of the Topical Meeting on Nonlinear Dynamics in Optical Systems*, Afton, OK, 4–8 June 1990.

R. L. McCrory, "New Research Trends in Inertial Confinement Fusion," to be published in the *Proceedings of the Topical Conference on Research Trends in Nonlinear and Relativistic Effects in Plasmas*, La Jolla, CA, 5–8 February 1990.

R. L. McCrory and C. P. Verdon, "Computer Modeling and Simulation in Inertial Confinement Fusion," to be published in *Il Nuovo Cimento*.

R. L. McCrory and C. P. Verdon, "Inertial Confinement Fusion: Computer Simulation," to be published as a book chapter in *Computer Applications of Plasma Science and Engineering*.

P. W. McKenty, C. P. Verdon, S. Skupsky, R. L. McCrory, D. K. Bradley, W. Seka, and P. A. Jaanimagi, "Numerical Modeling of Effects of Power Imbalance on Irradiation Nonuniformities," to be published in *Journal of Applied Physics*.

Conference Presentations

The following presentations were made at the Eighth APS Topical Conference on High-Temperature Plasma Diagnostics, Hyannis, MA, 6–10 May 1990:

T. J. Kessler, "ICF Laser Beam Focal Uniformity and Diagnostics."

M. Russotto and R. Kremens, "Measurement of Fuel Ion Temperatures in ICF Implosions Using Current-Mode Neutron Time-of-Flight Detectors."

R. C. Leary, "The OMEGA Laser Alignment System: A Real-Time VMS Application," presented at the US DECUS Spring 1990 Symposium, New Orleans, LA, 7–11 May 1990.

R. J. Hutchison and S. A. Kumpan, "Vendor and Subcontractor Management," presented at the OSA Regional Engineering Workshop, Rochester, NY, 10–11 May 1990.

The following presentations were made at the Seventh Topical Meeting on Ultrafast Phenomena, Monterey, CA, 14–17 May 1990:

H. E. Elsayed-Ali and J. W. Herman, "Picosecond Transient Surface Temperature Measurement by Reflection High-Energy Electron Diffraction."

H. E. Elsayed-Ali, T. Juhasz, G. O. Smith, and W. E. Bron, "Femtosecond Thermoreflectivity and Thermotransmissivity of Polycrystalline and Single-Crystalline Gold Films."

H. E. Elsayed-Ali, T. Juhasz, G. O. Smith, and W. E. Bron, "Femtosecond Thermomodulation of Single-Crystalline and Polycrystalline Gold Films."

D. D. Meyerhofer, "Observation of Barrier Suppression Ionization at Laser Intensities of 1 Atomic Unit," presented at the APS Division Meeting (invited talk), Monterey, CA, 21–23 May 1990.

S. Augst, D. D. Meyerhofer, J. Peatross, C. I. Moore, and J. H. Eberly, "Harmonic Generation in Noble Gases Using a High-Intensity 1-μm, 1-ps Laser," presented at IQEC '90, Anaheim, CA, 21–25 May 1990.

The following presentations were made at CLEO, Anaheim, CA, 21–26 May 1990:

H. E. Elsayed-Ali, T. Juhasz, and G. O. Smith, "Femtosecond Transient Thermomodulation of Thin Gold Films with Different Crystal Structures."

T. E. Gunderman, J.-C. Lee, T. J. Kessler, S. D. Jacobs, D. J. Smith, and S. Skupsky, "Liquid Crystal Distributed Polarization Rotator for Improved Uniformity of Focused Laser Light."

L. E. Kingsley and W. R. Donaldson, "Optical Probing of Semiconductor Carrier Dynamics."

Y. Lin, W. Seka, T. Kessler, W. Beich, D. Y. Park, H. Huang, and J. H. Eberly, "Properties of Realistic Bessel Beams."

G. G. Luther, C. J. McKinstrie, and A. L. Gaeta, "The Transverse Modulational Instability of Counterpropagating Light Waves," presented at the Topical Meeting on Nonlinear Dynamics in Optical Systems, Afton, OK, 4–8 June 1990.

The following presentations were made at the OSA Topical Meeting on Science of Optical Finishing, Monterey, CA 10–12 June 1990:

D. Golini and S. D. Jacobs, "Chemo-Mechanical Effects in Loose Abrasive Grinding of ULE."

S. D. Jacobs, "Unconventional Polishing" (invited talk).

A. Lindquist, S. D. Jacobs, and A. Feltz, "Surface Preparation Technique for Rapid Measurement of Sub-Surface Damage Depth."

G. Banas, F. V. Lawrence Jr., J. M. Rigsbee, and H. E. Elsayed-Ali, "Mechanical and Microstructural Modification of Welded Maraging Steel after Laser Shock Hardening," presented at MatTech '90, the First European East-West Symposium on Materials and Processes, Helsinki, Finland, 10–18 June 1990.

D. D. Meyerhofer, S. Augst, D. Strickland, and S. L. Chin, "Observation of Barrier Suppression Ionization at Laser Intensities of 1 Atomic Unit," presented at the Conference on Coherent Radiation Processes in Strong Fields, Washington, DC, 18–22 June 1990.

G. Banas, F. V. Lawrence, Jr., J. M. Rigsbee, and H. E. Elsayed-Ali, "Laser Shock Hardening of Welded Maraging Steel," presented at symposium on Surface Engineering: Current Trends and Future Prospects, University of Toronto, Toronto, Canada, 25–27 June 1990.